Computers and Geotechnics 174 (2024) 106648

Contents lists available at ScienceDirect

Computers and Geotechnics

journal homepage: www.elsevier.com/locate/compgeo

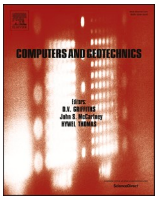

Research Paper

Evaluation of the Methods of Particle Morphology Characterization: CT Scanning, Digital Imaging and Light Microscopy

Karim Kootahi [a], Anthony Kwan Leung [a,*], Zhenliang Jiang [a], Jianbin Liu [a], Rui Qi [b], Sérgio D.N. Lourenço [b], Zhengshou Lai [c], Zhiwei Gao [d]

[a] Dept. of Civil and Environmental Engineering, Hong Kong Univ. of Science and Technology, Clear Water Bay, Kowloon, Hong Kong Special Administrative Region
[b] Department of Civil Engineering, The University of Hong Kong, Hong Kong Special Administrative Region
[c] School of Civil Engineering, Sun Yat-sen University, Shenzhen 518107 China
[d] James Watt School of Engineering, University of Glasgow, Glasgow G12 8QQ, UK

ARTICLE INFO

Keywords:
Morphology characterization
Sands
Digital imaging
Probability distributions

ABSTRACT

The morphology of granular materials can be characterized two or three-dimensionally by different measurement techniques such as micro-computed tomography (μCT), static and dynamic image analysis (SIA and DIA). Because there are fundamental differences in the working principles among these techniques, their efficacy in characterizing the morphology of granular particles needs to be precisely examined but has not yet been scientifically evaluated. In this study, a systematic evaluation of the efficacy of four DIA devices and a light microscope (LM) with reference to μCT was made by selecting statistically representative samples of three standard sands which covered a wide range of particle form and angularity. Morphological data of these sands were used and probability distributions obtained from the different imaging techniques were compared with μCT results using a precise quantitative measure based on the information theory. The results revealed that most of the DIA devices chosen were capable of providing accurate measurements for the coarse descriptors such as aspect ratio in sands across a broad particle size range, whereas some devices require improvement in their camera resolution to produce accurate measurements for fine sands. Modifying device configuration and/or computational algorithm to either use the captured image with the largest area or obtain an average from multiple random projections in the order of 100 can improve the accuracy of morphology characterization in DIA devices. LM with proper imaging and image processing can provide results comparable to μCT.

1. Introduction

Morphology of granular materials, which has been shown to directly influence their mechanical and hydraulic behavior (e.g., Cho et al. 2006; Payan et al. 2016; Nguyen and Indraratna 2020; Liang et al. 2022; Xiao et al. 2023; Li et al. 2024a,b), can be characterized in different dimensions (i.e., two- and three-dimensional, 2D and 3D) and at different scales (i.e., micro-, meso-, and macro-scales). Characterization at meso- and macro-scales using morphological descriptors that quantify the form or shape and angularity of particles can be made by different measurement techniques such as micro-computed tomography (μCT; e.g., Kong and Fonseca, 2018), dynamic image analysis (DIA; e.g., Fonseca et al. 2012), and static image analysis (SIA; e.g., Masad et al. 2005). Light microscopy (LM), which is a non-automatic SIA technique that requires separate processing stages including imaging, image processing and morphology quantification, has also been used for morphology characterization of sands in the literature (e.g., Cox and Budhu 2008). While μCT is an ideal technique to capture the full 3D particle surface geometries (Zheng et al. 2020) and thus to provide full 3D morphology characterization, DIA, SIA and LM can only provide 2D images. However, 3D morphology characterization using μCT usually requires the use of high-performance computing (HPC) systems and takes a much longer computation time to complete, especially when the sample size is medium to large [e.g., eight particles per hour for an HPC system, reported by Li et al. (2023)]. DIA and SIA, which both provide an automated process of morphology characterization from taking particle images to their processing and quantification, are much faster than μCT but cannot provide full 3D information. In addition to 2D characterization, DIA can characterize particle morphology pseudo-three dimensionally (pseudo-3D, or sometimes referred to as 2.5D), in which a number of particle projections in different orientations for the same particle (up to 30 in the

---

* Corresponding author.
E-mail address: ceanthony@ust.hk (A. Kwan Leung).

https://doi.org/10.1016/j.compgeo.2024.106648
Received 27 February 2024; Received in revised form 30 July 2024; Accepted 31 July 2024

Notation

APD	Absolute percentage deviation
DIA	Dynamic image analysis
KDE	Kernel density estimation
LM	Light microscopy (& Light microscope)
MV	Mean value
PDF	Probability density function
RSS	Representative sample size
SIA	Static image analysis
μCT	Micro-computed tomography
AR	Aspect ratio
$AR_{W/L}$	Width-to-length aspect ratio (or elongation index)
$AR_{T/L}$	Thickness-to-length aspect ratio (or flatness index)
A_{2D}	Surface area of the 2D particle projection
A_{3D}	Surface area of the 3D particle
A_c	Area of the minimum convex hull circumscribing the 2D particle projection
A_e	Surface of the sphere having the same volume as the particle
C_x	Convexity
D_{50}	Mean grain size
$\overline{D}_H$	PDF similarity (modified Hellinger distance)
f	Probability density function of variable X
L	Length of the particle
N	Number of particle corners
P_{2D}	Perimeter of the 2D particle projection
P_e	Perimeter of the circle having the same area as the 2D particle projection
R	Wadell roundness
$R_{ci,2D}$	Radius of the ith corner circle of the 2D particle projection
$R_{ci,3D}$	Radius of the ith corner sphere of the 3D particle
$R_{ins,2D}$	Radius of the largest inscribing circle of the 2D particle projection
$R_{ins,3D}$	Radius of the largest inscribing sphere of the 3D particle
$S_{A,3D}$	3D true sphericity or 3D surface area sphericity
T	Thickness of the particle
V	Volume of the 3D particle
V_c	Volume of the minimum convex hull circumscribing the 3D particle
W	Width of the particle

currently available devices) are used to determine the 2.5D morphological descriptors. This system of characterization has been referred to as "3D DIA" in some studies (Li and Iskander 2021; Li et al. 2023). In general, characterization using DIA at best is a 2D characterization equivalent to SIA and LM because, unlike SIA which targets characterization with utmost accuracy, DIA targets at high sample throughput and data reproducibility (Microtrac 2023). Compared to SIA in which the largest area projection of the particles is normally captured for a limited number of particles, DIA captures random projection of the particles for thousands to even millions of particles. Table 1 summarizes the descriptors of the first- and second-order morphological properties (i.e., form and angularity, respectively) obtained from these measuring techniques, either 2D, 3D or 2.5D.

Relatively speaking, DIA has received a wide popularity because of its ability to provide a fast and convenient means to characterize particle morphology (Li and Iskander 2021). However, due to the fundamental differences in the working principles among DIA, SIA and μCT, the efficacy of DIA as well as SIA for characterizing granular particles is yet to

Table 1
Definition of morphological descriptors selected for evaluation.

Descriptor		Formula	Reference	Graphical illustrations
First-order properties*	3D & 2.5D** aspect ratio (also known as thickness-to-length aspect ratio or flatness index)	$AR_{Z/L} = \frac{Z}{L}$ $AR_{Z/W} = \frac{Z}{W}$	Garboczi and Bullard (2017)	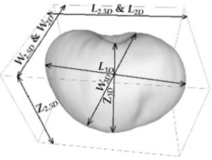
	2D & 2.5D aspect ratio (also known as width-to-length aspect ratio or elongation index)	$AR_{W/L} = \frac{W}{L}$	Fonseca et al. (2012)	
	3D surface area sphericity (also known as true sphericity)	$S_A = \frac{A_e}{A_{3D}}$	Wadell (1933)	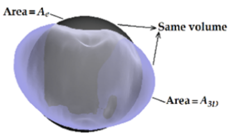
	2D & 2.5D perimeter sphericity	$S_P = \frac{P_e}{P_{2D}}$	Zheng and Hryciw (2015)	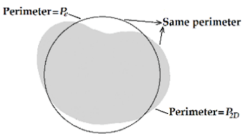
	3D convexity	$C_x = \frac{V}{V_c}$	Fonseca et al. (2012)	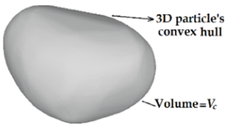
	2D & 2.5D convexity	$C_x = \frac{A_{2D}}{A_c}$	Fonseca et al. (2012)	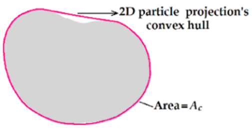
Second-order properties*	3D (local) roundness	$R = \frac{\sum_{i=1}^{N} \frac{R_{ci,3D}}{N}}{R_{ins,3D}}$	Wadell (1932)	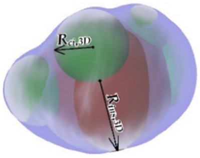
	2D & 2.5D (local) roundness	$R = \frac{\sum_{i=1}^{N} \frac{R_{ci,2D}}{N}}{R_{ins,2D}}$		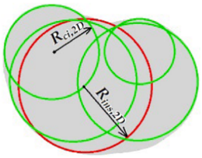

Notes: For definitions of the parameters used, see also list of symbols.

[*] First- and second-order morphological properties are measurable at macro- and *meso*-scales, respectively (Sandeep et al. 2023).

[**] 2.5D descriptors are the same as 2D ones except that mean or largest value of particle dimensions from a series of images is considered for computations.

be scientifically evaluated. Moreover, the efficacy of 2D and 2.5D techniques for morphology characterization also needs to be carefully evaluated before wide adoption. This evaluation is particularly important when determining the underlying probability distributions of morphological descriptors for inclusion in discrete element models (DEM; Nie et al. 2021) and 3D printed surrogates (Adamidis et al. 2020). To this end, Li et al. (2023), who CT-scanned individual particles of three sands with varying angularity and evaluated two DIA devices (one 2D device and one 2.5D device) in comparison to μCT, concluded that 2.5D DIA is viable for characterizing sphericity and convexity but not for roundness. Fonseca et al. (2012) used μCT scans obtained from resin-impregnated samples of a sand with varying particle shapes from spherical to highly non-spherical (Reigate sand from Southeast England) to characterize its morphology and compared their results with those obtained from a 2D DIA device. Fonseca et al. (2012) found that the 2D distribution of aspect ratio from DIA was intermediate between elongation and flatness indexes obtained from μCT ($AR_{W/L}$ and $AR_{Z/L}$ in Table 1), and did not correlate well with any of them. They also found that the range or distribution of values obtained from μCT for sphericity and convexity was markedly higher compared to that obtained from 2D DIA. Zhang et al. (2021) compared the results of their 3D characterization of Ottawa sand using μCT to 2D characterization using SIA for the same sand conducted by Zheng and Hryciw (2016). The study found a significant deviation between the probability density functions (PDFs) of both roundness and sphericity, leading to a rather different morphology classification.

The aforementioned studies, while providing insightful information, however, have several limitations. First, inconsistent methods and measures were used to compare the probability distributions obtained from the different imaging techniques. For example, all existing studies used visual qualitative methods to evaluate the similarities of PDFs (Li et al. 2023) and cumulative distribution functions (Zhang et al. 2021), which could be subjective and lacks preciseness. Second, the number of selected particles was random and rather small in some studies (e.g., 110–350 in Li et al. 2023; 170 in Zheng and Hryciw 2016); thus the derived distributions for different characterization methods may not be representative. Indeed, recent studies that used rigorous statistical analysis (e.g., information entropy) to obtain the representative sample size (RSS) needed for morphology characterization showed that RSS of about 140 and 500 particles are needed to capture the underlying mean and PDF of morphological data, even for sands with rounded particles (Kootahi et al. 2023a, b). Third, none of these studies considered the potential of a light microscope even though it may have higher accuracy than DIA. Finally, except for one study (Li et al. 2023), physically separated particles that do not require applying any algorithm to segment the contacting particles were not used in all test devices to make a fair comparison.

This study uses the concept of statistical representative samples to fairly and systematically evaluate the efficacy of particle morphology characterization using four DIA devices (two 2D devices and two 2.5D devices) and an LM device in comparison to μCT results for three standard sands that cover a wide range of particle form and angularity for geotechnical testing. The PDFs of morphological descriptors obtained from the various imaging techniques are compared with μCT results using a precise quantitative measure on the basis of the information theory. As several previous studies have already demonstrated the viability of DIA and SIA in characterizing the particle size distribution for granular materials (e.g., Altuhafi et al. 2013; Li and Iskander 2021; Li et al. 2023), only particle form and angularity are considered in this study. Furthermore, due to the limitations of DIA and LM, the third-order property (roughness) was not considered in this study. Widely used descriptors of particle form and angularity such as aspect ratio, convexity, sphericity, and roundness were selected for detailed investigation.

2. Materials and methods

2.1. Test devices and their working principles

Four DIA devices (DEV), an LM and a μCT scanner were selected for evaluation. The list of the devices along with some main and relevant features of each device is given in Table 2.

In X-ray CT scanning, the sample of particles, placed on a rotating table, is radiated with an X-ray source, while a digital detector captures 2D X-ray projections at predetermined increments as the sample rotates 360° (Li et al. 2023). The raw projection images are then rendered to obtain 3D volume reconstruction, followed by some image processing steps to reduce the noise when necessary and segment different phases. The segmented individual particles are then used to extract the boundary voxels of each particle so that the 3D morphological descriptors can be computed.

As shown in Fig. 1, all four DIA devices considered use a particle feeder that is composed of a feed hopper connected to a vibrating tray, where the height between the hopper and tray is adjustable to allow controlling the feeding rate. The hopper is filled with the test material, and the adjustable height between the hopper and tray transports the particles of the test material to the vibrating tray, where particles can be separated and a constant flow of particles can be fed for imaging as the particles fall from the tray to the sensing zone. In all four selected DIA devices, the sensing zone is comprised of one or two high frame-rate (HFR) cameras, a light source located at their focal distance, and a unit for collecting the test materials. The imaging in the sensing zone is conducted in the so-called viewing area where direct illumination required for capturing high-quality images with good contrast is available. However, major differences exist amongst the four devices, in terms of lighting system, number of cameras, camera resolution, framing rate, and the computing algorithms to obtain the morphological data (see Table 2). DEV 4 employs pulsed laser light with extremely short exposure time of a sub-nanosecond that prevents motion blur of the particles in the captured images, while DEV 1, DEV 2 and DEV 3 use ultrabright LED stroboscopic light with longer exposure time that provides relatively less sharp grey-scale images. In DEV 1 and DEV 4, only one camera is used to detect the particles, while DEV 2 and DEV 3 use two cameras which share the same focal plane to detect the particles; in the latter case, one camera with a lower resolution registers larger particles, while a higher resolution zoom camera registers small particles. The two cameras together provide a frame rate of 250 and 300 frames per second (FPS) in DEV 2 and DEV 3, respectively. The framing rate in devices DEV 1 and DEV 4 is 100 and 175 FPS, respectively. The captured images can be visualized in real time by the device's built-in software, which processes the images by extracting the outline of each particle and using them to compute some widely used morphological descriptors such as those listed in Table 1. In the 2.5D devices DEV 1 and DEV 2, every particle traveling downward is tracked since entering the viewing area until leaving it; this technique provides a series of images at different orientations for each particle. The tracking is made by an algorithm that utilizes multiple sequential images containing a specific particle by the following manner: the particle is given a label right after entering the viewing area and its location over time is estimated. The estimated location is then used to track the particle in the next captured image and so on until the particle leaves the viewing area. Devices DEV 1 and DEV 2 are capable of tracking up to 30 images for each particle. In the 2D devices DEV 3 and DVE 4, however, no particle tracking can be made and thus images captured in the viewing area for each particle have to be considered separately. DEV 1, DEV 2, and DEV 3 provide the descriptors of both the first-order morphological properties (e.g. aspect ratio, sphericity, convexity) and the second-order ones (i.e. local roundness). However, DEV 4 does not provide any descriptor of the second-order morphological property due to the limitation in its built-in software. Yet, images captured by this device can be analyzed using a third-party software or code to obtain the parameters required for

Table 2

List of the imaging devices chosen for evaluation and their main features.

Imaging technique	Device name/ model	Resolution (μ)	Lighting (and frame rate)	Applicability	Morphological descriptors provided
μCT	Nano Voxel-3000	3[1]	X-ray (adjustable to 1800 SPR[2])	–	None
DIA	DEV 1 (2.5D)	15	LED (100 FPS[3])	22 μm–35 mm (>150 μm)[4]	20 descriptors including $AR_{Z/L,2.5D}$, $AR_{W/L,2.5D}$, $C_{x,2.5D}$, $S_{P,2.5D}$, $R_{2.5D}$
	DEV 2 (2.5D)	7	LED (250 FPS)	20 μm–30 mm	13 descriptors including $AR_{Z/L,2.5D}$, $AR_{W/L,2.5D}$, $C_{x,2.5D}$, $S_{P,2.5D}$, $R_{2.5D}$
	DEV 3 (2D)	1	LED (300 FPS)	0.8 μm–8 mm	13 descriptors including $AR_{W/L,2D}$, $C_{x,2D}$, $S_{P,2D}$, R_{2D}[5]
	DEV 4 (2D)	4	Laser (175 FPS)	1.8 μm–4 mm (>40 μm)[4]	4 descriptors including $AR_{W/L,2D}$, $C_{x,2D}$, $S_{P,2D}$
LM	Topcon TMM-13OZ	1[1]	Halogen lamp (manual)	–	None

Notes

[1] Maximum achievable resolution.

[2] Steps per rotation.

[3] Frames per second.

[4] Recommendation in the literature for particle shape measurement.

[5] Convexity is computed as. $\sqrt{A_{2D}/A_c}$.

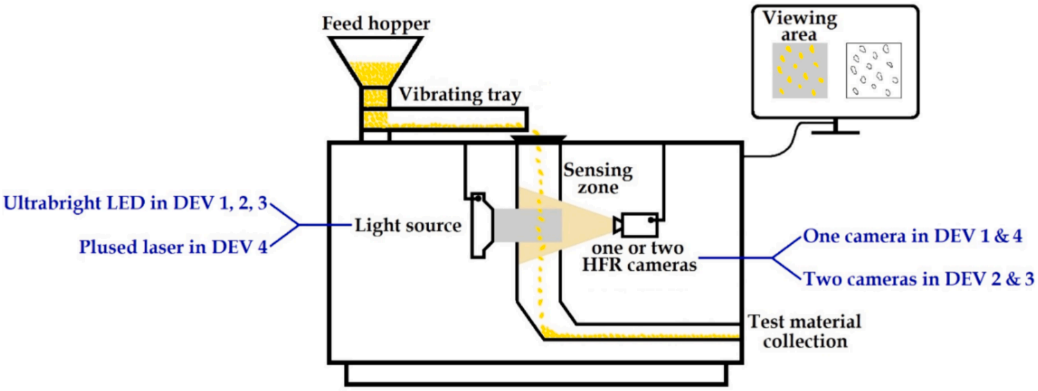

Fig. 1. Schematic representation of the general working principles of the selected DIA devices along with their main features.

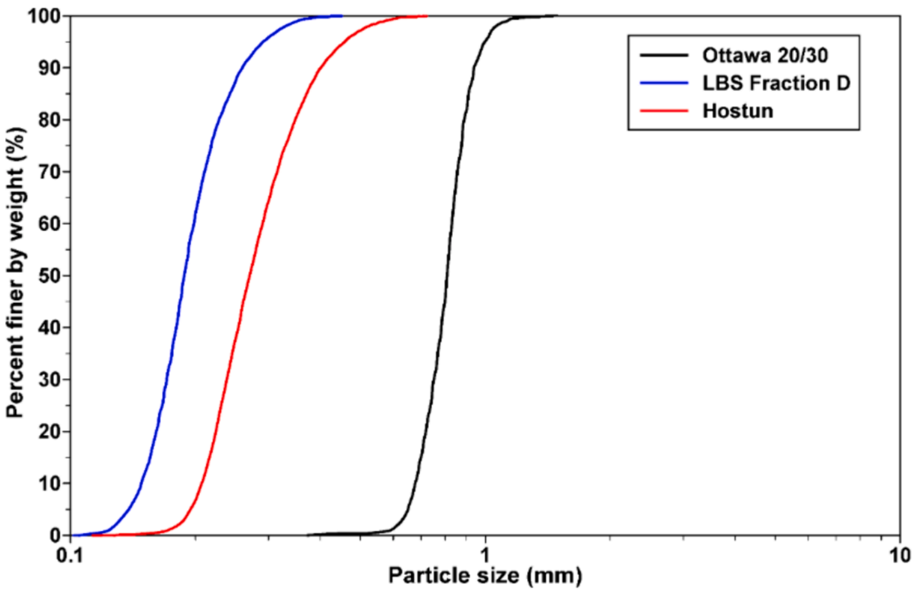

Fig. 2. Particle size distribution of the three standard sands chosen for investigation.

computing descriptors of the second-order morphological property. The computation method of roundness in DEV 1, DEV 2, and DEV 3 follows the definition proposed by Wadell (1932), with a difference that DEV 1 uses a manually adjustable threshold to differentiate the exact particle's edges and corners from the background. Meanwhile, DEV 2 and DEV 3 use automatic particle threshold search to identify particle's edges and corners and fit circles to them so that $R_{ci,2D}$, $R_{ins,2D}$, and N can be quantified (Table 1). In devices DEV 1 and DEV 2, mean values of particle area and perimeter from a series of images captured at different orientations (i.e., up to 30 tracked particle images) are used to compute S_P, C_x, and R, while the largest value of particle dimensions from the same series of images is considered for computing $AR_{Z/L}$ and $AR_{W/L}$.

In LM, the particles in the sample are illuminated by light bulbs, light-emitting diodes (LEDs) or lasers and the reflected light from the particles is received by an optical system. The LM digital images obtained are then converted to binary so that the outlines of individual particles and thus 2D morphological descriptors can be determined.

2.2. Test sands and testing procedures

Three standard silica sands that have been extensively studied in geotechnical literature were selected for evaluation, including Ottawa 20/30 sand, Leighton Buzzard sand (LBS) fraction D, and Hostun sand (Ottawa, LBS and Hostun, for short hereafter). The particle size distribution of the three sands is shown in Fig. 2; the minimum particle size of the three sands was 0.11 mm which is well within the applicability limit of all the selected DIA devices (Table 2). The mean particle size (D_{50}) of Ottawa, LBS and Hostun was 0.81, 0.19, and 0.27 mm, respectively. Their particle angularity and form belong to different classes based on the classifications proposed by Powers (1953) and Krumbein and Sloss (1963); more specifically, Ottawa has well-rounded to rounded particles with circular shapes, while Hostun particles are angular to subrounded with semicircular shapes. LBS is in between these two sands as it has subrounded to rounded particles with semicircular shapes. Thus, the choice of sands covered a wide range of particle form and angularity for evaluating the different imaging techniques.

The number of particles selected for CT scanning was more than 600 for each type of the tested sands, of which 600 particles were selected for 3D volume reconstruction and morphology quantification. This selection was obtained based on the algorithm developed by Kootahi et al. (2023a) which determines an RSS required to capture the underlying PDFs of morphological data of sands, including Hostun and some others that are more spherical than the Ottawa tested in the present study (e.g., Caicos sand). The algorithm application to the two sands is presented in Appendix A, and the results show that the RSS needed for capturing PDFs of the 3D true sphericity of Hostun and Caicos sands is 500 and 592, respectively. It is noted that descriptors of second-order properties such as roundness require smaller RSS because of their less skewed distributions (e.g., normally distributed; Tunwel et al. 2018). Thus, a selection of 600 would ensure capturing the underlying PDFs for the sands considered in this study.

To maximize the accuracy of 3D volume reconstruction of the particles during CT scanning and to avoid over-segmentation during image processing (Yang et al. 2022), the particles were physically separated following the method described in Li et al. (2023), including: (1) evenly spraying the sand particles without overlapping as much as possible on a layer of packaging tape with a width of 20 mm; (2) using another tape layer to fix the positions of the particles; and (3) wrapping the tape with sandwiched particles around a plastic cylinder tube with a diameter of 15 mm and a height of 20 mm. This cylindrical sample was scanned and its resulting imaging data were analyzed using the reconstruction software Voxel Studio Recon (Sanying Precision Instruments, Co., Ltd., China) by the following procedures: (1) radiating the sample in 1800 steps per rotation with a scanning voltage and a current of 105 kV and 200 μA, respectively; (2) reconstructing the 2D tomograms to a 3D 16-bit image; (3) generating a binarized image by applying global thresholding along with the use of median filter to reduce the noise; and (4) applying the watershed algorithm and the marching cubes algorithm to extract the segmented individual particles and to compute polygonal isosurfaces of the particles. The resulting particle image resolution for Ottawa, LBS and Hostun was 12.4, 5.8, and 7.4 μm/voxel, respectively, which are all higher than that adopted by Li et al. (2023) (i.e., 14 μm/voxel) who tested three sands with particle sizes larger than those considered in the present study (D_{50} ranging from 0.53 to 2.40 mm).

The number of particles selected for LM was also more than 600 for each of the tested sands; similarly, 600 of them were selected for image processing and subsequent morphology quantification. A detailed yet easy-to-follow procedure was developed to improve the quality of acquired data, including: (1) placing the sand particles on a microscope slide that overlaid a contrasting background (i.e., a black sheet); (2) gently nudging the slide to separate the particles as much as possible and to ensure imaging the maximum particle projection which best represents 3D morphological descriptors (Rorato et al. 2019); (3) taking a microscope image such that a particle length of at least 250 pixels for the smallest particle of each sand can be obtained to prevent the effects of image resolution on the subsequent morphology quantification (Sun et al. 2019); (4) segmenting the image in an open-source software *Fiji* through image-specific selection of thresholds, instead of using only the widely used Otsu threshold for all the taken images; and (5) using Trainable Weka Segmentation from *Fiji* when none of the available thresholds provided a satisfactory result (i.e., not detecting all particle's outlines in an image). The resulting image resolution for Ottawa, LBS and Hostun was 4.2, 1.7, and 1.6 μm/voxel, respectively, which is comparable to that of DEV 3 and DEV 4.

Different sample weights were used for DIA, ranging from 5 g for LBS to 75 g for Ottawa. The number of particles imaged by the DIA devices ranged from 30,997 to 2,581,285. While DEV 1 took 13 to 21 images in different orientations from each particle, the number of images taken by DEV 2 was not reported but the device can take up to 30 images in different orientations. DEV 3 and DEV 4 were both 2D DIA and thus images captured in different orientations for each particle were reported as separate particle images.

2.3. Quantitative measures for comparisons

To quantify the similarity among the distributions of morphological descriptors obtained from the different imaging techniques, Hellinger distance (HD) on the basis of information entropy was used. HD is a relative entropy measure that has been used as a precise quantitative measure (Krzanowski 2003; Ruggeri et al. 2021) which can quantify a range of dissimilarities between any two PDFs, whether they are symmetric and/or asymmetric (Gardner et al. 2019). Relative entropy between two distributions, f_1 and f_2, measures the inefficiency of assuming a priori that the PDF is f_2 when the true underlying PDF is f_1 (Gokhale and Kullback, 1978). The HD between two PDFs, f_1 and f_2, can be defined as follows to quantify 'PDF similarity' (Kootahi et al. 2023b):

$$\overline{\mathrm{D}}_{\mathrm{H}}(f_1,f_2) = 1 - \sqrt{\frac{1}{2}\int\left(\sqrt{f_1} - \sqrt{f_2}\right)^2 dx} \tag{1}$$

HD is symmetrical [i.e., $\overline{\mathrm{D}}_{\mathrm{H}}(f_1,f_2) = \overline{\mathrm{D}}_{\mathrm{H}}(f_2,f_1)$] and bounded on both sides with $\overline{\mathrm{D}}_{\mathrm{H}} \in [0, 1]$ in which $\overline{\mathrm{D}}_{\mathrm{H}}$ reaches zero when f_1 and f_2 have zero similarity and it is equal to 1 when the two PDFs are identical. Using Equation (1) requires the PDFs f_1 and f_2 be captured objectively without any presumption on the distribution type of the underlying data. Thus, density functions were estimated using kernel density estimation (KDE; Sheather 2004), in which the widely used Gaussian function and Sheather–Jones plug-in (Sheather and Jones 1991) were used for kernel function and optimal bandwidth, respectively.

On the other hand, absolute percentage deviation (APD), as defined in the following equation, was used to quantify the similarity between the mean value of a morphological descriptor obtained from a device (MV_{dev}) compared with that obtained from µCT ($MV_{\mu\text{CT}}$):

$$\text{APD} = 100 \times \frac{|MV_{\text{dev}} - MV_{\mu\text{CT}}|}{MV_{\mu\text{CT}}} \tag{2}$$

2.4. Selected morphological descriptors and their computation

The morphological descriptors of the first- and second-order properties considered in this study are summarized in Table 1. More specifically, the descriptors selected to characterize particle form include aspect ratio (AR), surface area or true sphericity (S_A), and convexity (C_x), whereas one descriptor was selected for angularity characterization which is the (local) roundness (R) as defined by Wadell (1932, 1933). Computation of 3D morphological descriptors for µCT reconstructed surface geometries was carried out using special algorithms developed in MATLAB and followed the method used in Lai and Chen (2019). More specifically, to obtain the two independent 3D aspect ratios $AR_{W/L}$ (width-to-length aspect ratio or elongation index) and $AR_{T/L}$ (thickness-to-length aspect ratio or flatness index; see Table 1), three Feret diameters corresponding to the three principal axes are calculated. The calculation involves the determination of a rotation matrix that defines the directions of the particle's principal axes and multiplying it to align the principal axes of the particle with the Cartesian axes. For computing 3D roundness based on Wadell's definition, first the radius of the maximum inscribed sphere ($R_{ins,3D}$) is obtained by computing the

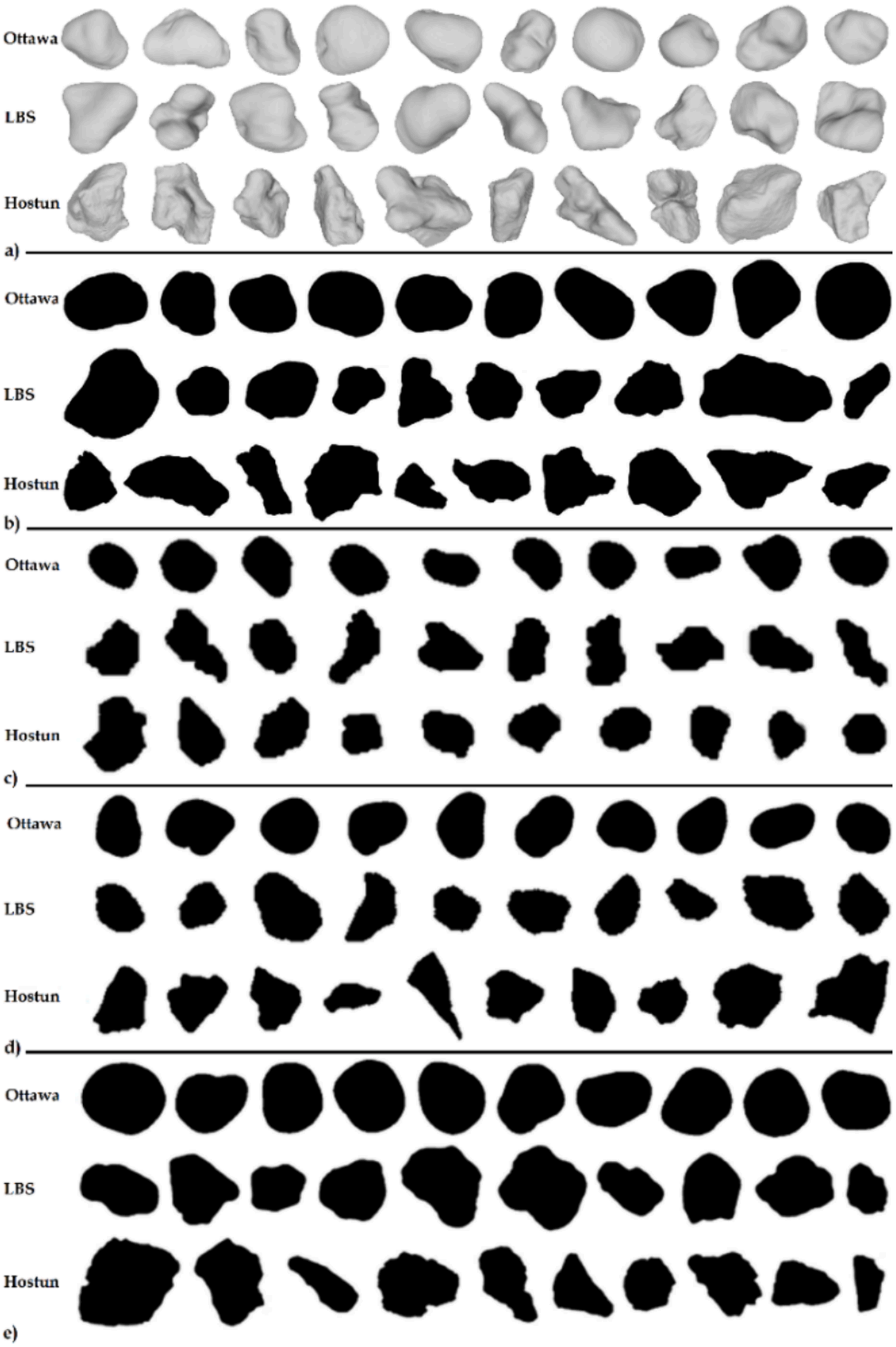

Fig. 3. Example images of 10 particles of each sand type captured by (a) µCT; (b) LM; (c) DEV1; (d) DEV 2 & 3; and (e) DEV 4. Note: the size of particles of the three sands were different but all have been rescaled to the same size here to facilitate comparison.

minimum radial distance of all vertexes on the particle surface to the particle centroid. Then, following the method introduced by Zhou et al. (2018), acceptable and unacceptable corners are detected by comparing $R_{ins,3D}$ with the maximum curvature at a corner.

The morphological descriptors obtained from DIA devices are summarized in Table 1. A subscript is used for each descriptor to indicate the number of dimensions (either 2D or 2.5D). Computation of 2D morphological descriptors for LM images was carried out using the MATLAB code developed by Zheng and Hryciw (2015). Among the several existing definitions of 2D sphericity, one that is deemed to have the potential to best represent the 3D true sphericity was selected, namely 2D perimeter sphericity ($S_{P,2D}$ in Table 1).

3. Results and discussion

3.1. Example images from different devices

Fig. 3(a) to 3(e) show typical example images of ten particles for the three sands taken by the five different devices. It visually appears that, compared with other DIA devices, DEV 4 captured the highest quality images because it captured more accurate and sharper particle boundaries. This result is not surprising because the laser illumination technique employed in the imaging process of this device returns more well-defined edges (Li et al. 2023). Yet, the images taken by DEV 4 were not comparable with those by LM, in which all the particle boundaries seem to be also captured accurately. However, obtaining sharper boundaries of particles does not ensure accurate morphology quantification because proper smoothing of the particle surfaces (i.e., removing particle roughness) is another factor that would affect the morphology quantification for descriptors such as local roundness. A more detailed discussion is given later.

3.2. First-order morphological properties

3.2.1. Aspect ratio

Fig. 4 shows the PDFs of the aspect ratio of Ottawa [Fig. 4(a)], LBS [Fig. 4(b)], and Hostun [Fig. 4(c)]. The corresponding values of HD that quantify the PDF similarities for $AR_{T/L}$ and $AR_{W/L}$ in Fig. 4 are summarized in Table 3. Note that only DEV 1 could provide $AR_{T/L}$. Among all the sands being tested, the PDF of $AR_{T/L}$ is nearly symmetrical and similar to that of $AR_{W/L}$ but shifted towards the left-hand side (i.e., smaller $AR_{T/L}$ values compared to $AR_{W/L}$) even for rather spherical and well-rounded Ottawa particles. While most of the DIA devices provided PDFs of $AR_{W/L}$ comparable with the µCT results, only the $AR_{T/L}$ for Ottawa obtained by DEV1 has a comparable PDF with that by µCT, with a similarity of up to 83 %. However, the capability of DEV 1 declined to HD values of 0.71 and 0.63 for LBS and Hostun, respectively.

In terms of $AR_{W/L}$, most of the DIA devices provided PDFs that well resembled the µCT results because the width-to-length aspect ratio is the coarsest descriptor of particle morphology, which requires the lowest image resolution (Sun et al. 2019) and its computation is quite straightforward (e.g., not requiring computation of particle area or perimeter). Yet, DEV 1 showed a rather poor performance for this simple descriptor when applied to LBS (with an HD of 0.60). Note that the 2D images of LBS taken using LM had a higher resolution of 1.7 µm which resulted in obtaining quite high PDF similarity between $AR_{W/L,3D}$ and $AR_{W/L,2D}$ for this fine sand (HD=0.91). The resolution of the camera employed in DEV 1 was relatively low (15 µm) and its camera had the slowest framing rate amongst all the DIA devices chosen for investigation (two to three times slower). Thus, it may be advisable to use a higher speed camera with improved resolution in this particular device to potentially reduce the discrepancy obtained between $AR_{W/L,3D}$ and $AR_{W/L,2D}$ in fine sands. Indeed, Li et al. (2023) showed that morphology characterization using a 2.5D device in their study can be improved by employing a camera of higher resolution. Among the PDFs obtained for $AR_{W/L}$, LM provided the most similar PDFs to the µCT for all the sands tested, with rather high HD values of 0.91 – 0.96. LM is a static method of imaging and with the help of the procedure followed in this study, it was possible to have a view of the particles normal to their plane of greatest stability and thus capture the maximum particle projections. Overall, except DEV 1, all the imaging techniques evaluated, whether static or dynamic, can provide a reliable PDF for $AR_{W/L}$ but not for $AR_{T/L}$.

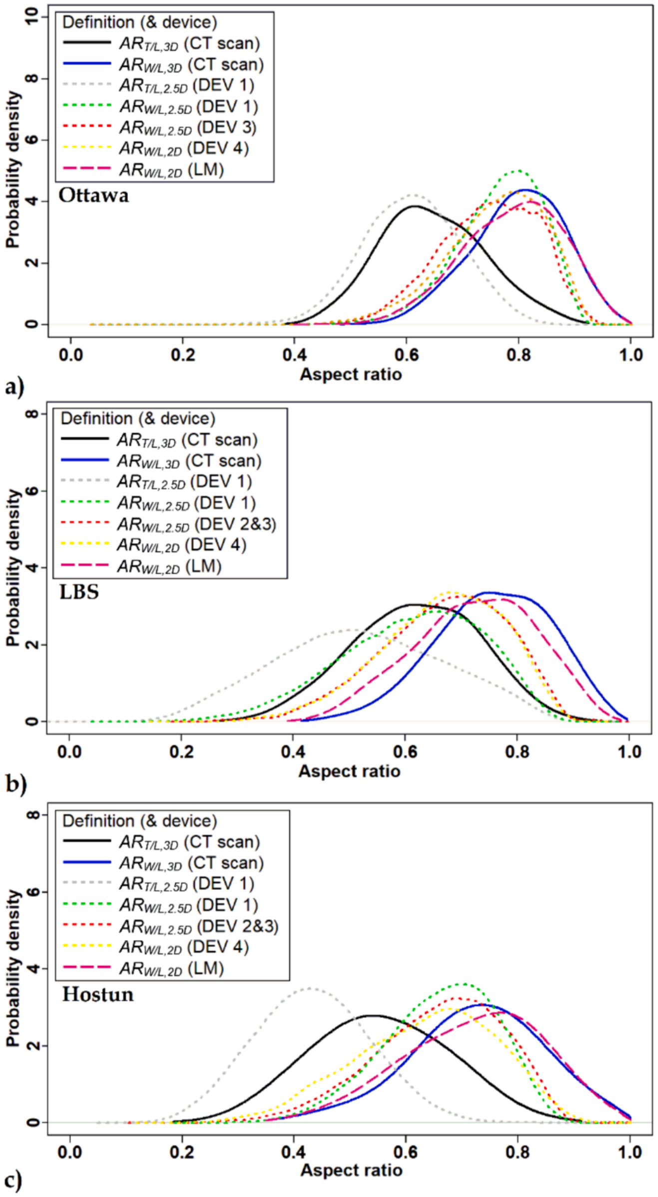

Fig. 4. PDFs of 3D aspect ratio and its 2D and 2.5D proxies from different devices for: (a) Ottawa; (b) LBS; and (c) Hostun.

The box plot shown in Fig. 5 summarizes the mean values of $AR_{W/L}$ obtained from different devices and the corresponding APDs. The $AR_{W/L}$ obtained by µCT was considered as the reference. The trends observed from the mean values followed those obtained for the PDFs. LM exhibited the smallest APD, ranging between 0.9 % and 3.9 %. DEV 1 showed a trend of increasing APD as the size of the particles being tested decreased (i.e. APDs increased from 4.2 % for Ottawa to 9.3 % for Hostun and eventually to 18.5 % for LBS) because of the inadequacy of the camera resolution. DEV 4 also had somewhat large APDs (up to 12.9 %). DEV 2 and DEV 3 have moderate deviations in the range of 6.6 % to 10.9 %. Mean values of morphological descriptors are mainly used in shape and angularity classification. For example, intercept sphericity,

Table 3
Hellinger distances for similarities of PDFs between 3D aspect ratio and its 2D proxies from different devices.

Ottawa 20/30	$AR_{T/L,3D}$ (CT scan)	$AR_{W/L,3D}$ (CT scan)	$AR_{W/L,2.5D}$ (DEV 2)	$AR_{T/L,2.5D}$ (DEV 1)	$AR_{W/L,2.5D}$ (DEV 1)	$AR_{W/L,2D}$ (DEV 4)	$AR_{W/L,2D}$ (LM)
$AR_{T/L,3D}$ (CT scan)	1	0.50	–	0.83*	–	–	–
$AR_{W/L,3D}$ (CT scan)		1	0.79	–	0.80	0.81	0.96
$AR_{W/L,2.5D}$ (DEV 2)			1	–	0.89	0.93	0.82
$AR_{T/L,2.5D}$ (DEV 1)				1	–	–	–
$AR_{W/L,2.5D}$ (DEV 1)					1	0.93	0.81
$AR_{W/L,2D}$ (DEV 4)						1	0.83
$AR_{W/L,2D}$ (LM)							1

LBS Frac D	$AR_{T/L,3D}$ (CT scan)	$AR_{W/L,3D}$ (CT scan)	$AR_{W/L,2.5D}$ (DEV 2&3)**	$AR_{T/L,2.5D}$ (DEV 1)	$AR_{W/L,2.5D}$ (DEV 1)	$AR_{W/L,2D}$ (DEV 4)	$AR_{W/L,2D}$ (LM)
$AR_{T/L,3D}$ (CT scan)	1	0.70	–	0.70*	–	–	–
$AR_{W/L,3D}$ (CT scan)		1	0.74	–	0.60	0.72	0.91
$AR_{W/L,2.5D}$ (DEV 2&3)**			1	–	0.83	0.97	0.81
$AR_{T/L,2.5D}$ (DEV 1)				1	–	–	–
$AR_{W/L,2.5D}$ (DEV 1)					1	0.83	0.65
$AR_{W/L,2D}$ (DEV 4)						1	0.79
$AR_{W/L,2D}$ (LM)							1

Hostun	$AR_{T/L,3D}$ (CT scan)	$AR_{W/L,3D}$ (CT scan)	$AR_{W/L,2.5D}$ (DEV 2&3)**	$AR_{T/L,2.5D}$ (DEV 1)	$AR_{W/L,2.5D}$ (DEV 1)	$AR_{W/L,2D}$ (DEV 4)	$AR_{W/L,2D}$ (LM)
$AR_{T/L,3D}$ (CT scan)	1	0.56	–	0.64*	–	–	–
$AR_{W/L,3D}$ (CT scan)		1	0.77	–	0.75	0.75	0.96
$AR_{W/L,2.5D}$ (DEV 2&3)**			1	–	0.93	0.92	0.77
$AR_{T/L,2.5D}$ (DEV 1)				1	–	–	–
$AR_{W/L,2.5D}$ (DEV 1)					1	0.87	0.74
$AR_{W/L,2D}$ (DEV 4)						1	0.76
$AR_{W/L,2D}$ (LM)							1

* 3D aspect ratio is only compared between µCT and DEV 1 as well as between the two aspect ratios obtained from µCT (i.e., $AR_{T/L,3D}$ and $AR_{W/L,3D}$).

** Distribution of $AR_{W/L,2.5D}$ obtained from DEV 2 was exactly the same as the distribution of $AR_{W/L,2D}$ from DEV 3.

which has the same definition as $AR_{W/L}$, was used by Krumbein and Sloss (1963) to classify particle shapes. Using the mean values of $AR_{W/L}$ from µCT as reference values along with this classification system it was found that the classification success rate (*CSR*) for DEV 1, 2, 3 and 4 was 66 % while it was 100 % for LM, where the *CSR* was calculated as the number of correctly classified samples divided by the total number of samples.

3.2.2. *Sphericity*

Fig. 6 shows the PDFs of 3D true sphericity ($S_{A,3D}$) obtained by µCT and its 2D proxy $S_{P,2D}$ obtained from different devices for Ottawa [Fig. 6(a)], LBS [Fig. 6(b)], and Hostun [Fig. 6(c)]. The corresponding HD values, quantifying the PDF similarities in Fig. 6, are summarized in Table 4. The PDFs of $S_{P,2D}$ obtained by LM are the most similar to those of $S_{A,3D}$ for all the sands tested and have the highest similarity with the µCT results. The HD values in Table 4 confirm that among all the devices evaluated, the PDFs obtained from LM have moderately high HD values in the range of 0.76 to 0.85 and have the highest distribution similarity to µCT results. DEV 1 overestimated the $S_{P,2D}$ for Ottawa and Hostun sands (when compared with the µCT results) because the camera resolution of this device was the lowest among the other evaluated DIA devices (Table 2). The best DIA device for this morphological descriptor was DEV 3 which returned the highest HD values (ranged between 0.60 and 0.80). The results show that the PDFs derived from the DIA devices can be rather different, returning PDF similarities as low as 38 %. Except for DEV 4, while no significant differences can be found in the upper tails of PDFs obtained for $S_{A,3D}$ and $S_{P,2D}$ for any of the imaging methods, the difference in the lower tails was remarkably high for all the DIA devices. Contrary to the µCT results which indicate values of $S_{A,3D} \geq 0.6$ for the three sands, the lower tails of the PDFs obtained using the DIA technique indicate the presence of highly non-spherical particles with $S_{P,2D}$ as low as 0.3 even in Ottawa sand. Such differences would lead to a rather different morphology classification for a specific sand. This difference could be partly related to the fundamental difference between the method of determining the particle sphericity using 3D volumes and external 2D projections, or/and the different working principles adopted by the different DIA devices because LM provided similar lower tails with the µCT results. The use of 2D maximum projections instead of random projections employed by the DIA devices could significantly improve the estimates of $S_{P,2D}$.

Further analyses were carried out using the µCT results to elucidate the influence of particle projection on the $S_{P,2D}$ determination. The 3D volumes of thirty particles reconstructed by the µCT were randomly selected from each tested sand so the $S_{A,3D}$ obtained can be compared with $S_{P,2D}$ determined for both the 2D maximum particle projection and two 2D random projections. Fig. 7 shows the results of three example particles of each. Also shown in the figure are volume-equivalent spheres and area-equivalent circles for 3D volumes and 2D projections, respectively. Note that $S_{A,3D}$ is the ratio of the area of the sphere shown in the figure to the particle's area while $S_{P,2D}$ is the ratio of the

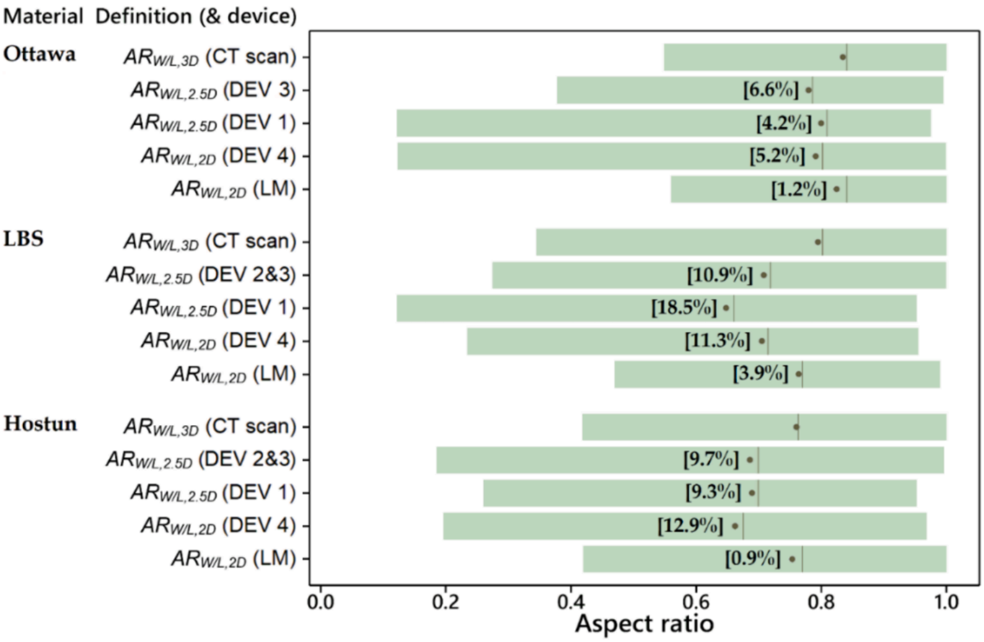

Fig. 5. Box plot of 3D aspect ratio and its proxies obtained from different devices. Note: points and lines indicate mean and median values, respectively, and the values in the brackets are APD.

perimeter of the circle shown to the particle's perimeter. Except for the three particles (L2, L3, and H2) the $S_{P,2D}$ obtained from the case of maximum projections better represented the $S_{A,3D}$. The more elongated the particle, the more projection-dependent its $S_{P,2D}$. For example, it varied largely in particles O3, L2, and H2. Fig. 8(a) and 8(b) show how $S_{A,3D}$ of all 90 particles correlates with $S_{P,2D}$ obtained from the maximum projection and randomly-oriented projections, respectively. Also shown in the figures is the correlation obtained by Sandeep et al. (2023) who sought for such a correlation using mean values from 100 random projections. First, $S_{P,2D}$ obtained from maximum projections overestimated $S_{A,3D}$ in most of the cases by 4 % to 15 %. Second, while $S_{P,2D}$ obtained from maximum projection was highly correlated with $S_{A,3D}$ [with a high correlation coefficient ρ of 0.89; Fig. 8(a)], a mild to weak correlation for $S_{P,2D}$ from the two random projections [$\rho = 0.64$ and 0.70 in Fig. 8(b)] can be found. Interestingly, the trend obtained from maximum projections based on 90 particles in this study [Fig. 8(a)] is quite similar to that obtained by Sandeep et al. (2023), which implies that $S_{P,2D}$ from the maximum projection might be considered equivalent to the mean value from 100 random projections for the same particle. Rorato et al. (2019) also found a significantly higher correlation between $S_{A,3D}$ and $S_{P,2D}$ for maximum particle projection ($\rho = 0.83$) compared with the case of using a single random projection ($\rho = 0.55$).

From Fig. 8(b), significant underestimation or overestimation of $S_{A,3D}$ occurred when using a single random projection; the corresponding correlation between $S_{A,3D}$ and $S_{P,2D}$ were quite different from that obtained by maximum projections and that by Sandeep et al. (2023). The discrepancy is mostly attributed to the highly non-spherical particles found in the three tested sands because they can have quite different $S_{P,2D}$ values depending on the selected projection. It may be advisable to use either the maximum projection or mean value from multiple random projections (in the order of ~ 100) to determine $S_{P,2D}$. However, neither of these is feasible in the DIA devices evaluated in this study. While the 2D DIA devices considered (i.e., DEV 3 and DEV 4) cannot perform particle tracking which means capturing the maximum projection for every particle is impossible, the 2.5D DIA devices can take a significantly smaller number of images from each particle (only up to 30 images in DEV 1 and DEV 2). Yet, these images in different orientations taken from a single particle may be enough to capture its maximum particle projection; thus, it may be suggested to modify the computational algorithm of 2.5D DIA devices so that $S_{P,2D}$ can be determined based on the captured image with the largest area instead of averaging from up to only 30 captured images. Indeed, these devices use this logic to compute the particle dimensions L, W, and Z but not $S_{P,2D}$. Another suggestion would be to enlarge the viewing area in the configuration of DIA devices so that the number of images captured for each particle can be increased from up to 30 to up to 100. Finally, it is noted that the maximum projection obtained computationally in this section is slightly different from the projection captured using LM (i.e., displaying the particles on a flat surface). Nonetheless, Suh et al. (2017) showed that computationally obtained 2D morphological descriptors are within 5 % of the values obtained from particles displayed on a flat surface. The gentle nudging of the microscope slide a few times as employed in this study may have resulted in more similar $S_{P,2D}$ values. In agreement with the computational results in Fig. 8(a) (i.e., tendency for slight overestimation of $S_{A,3D}$ when maximum projections are used), the PDFs obtained using LM showed a slight overestimation of $S_{A,3D}$ in the Ottawa and LBS sands, while indicating a slight underestimation in Hostun which cannot be explained by the trend sought in Fig. 8(a).

To further investigate the effect of number of particle projections on the computation accuracy of sphericity and compare them with the maximum particle projection, a theoretical computation was carried out using the μCT reconstructed 3D volumes of 90 particles (i.e. 30 particles from each tested sand). Random projection of each particle was obtained for a wide range of selected number of random projections (i.e., 5, 10, 15, 20, 25, 30, 40, 50, 60, 80, 100, and 150). Mean value of 2D sphericity ($S_{P,2D}$) was also computed for these random particle projections. Fig. 9 shows the percentage deviation of $S_{P,2D}$ from 3D true sphericity ($S_{A,3D}$) for the different numbers of random projections used and for the maximum particle projection. Notably, deviations were negative in most of the cases (i.e., overestimation of $S_{A,3D}$) so absolute percentage deviations are presented in the figure. The data in the figure was categorized into three classes of $S_{A,3D}$, namely $0.70 < S_{A,3D} < 0.80$, $0.80 < S_{A,3D} < 0.90$, $0.90 < S_{A,3D} < 1.00$. Two typical particles from each tested sand were presented for brevity. First, for all classes of $S_{A,3D}$, the percentage deviation reduced with increasing number of random projections from 5 to 100 but for larger number of projections (i.e., 150), negligible change in the percentage deviation was found. In other words, the accuracy of estimating $S_{A,3D}$ increased with increasing number of

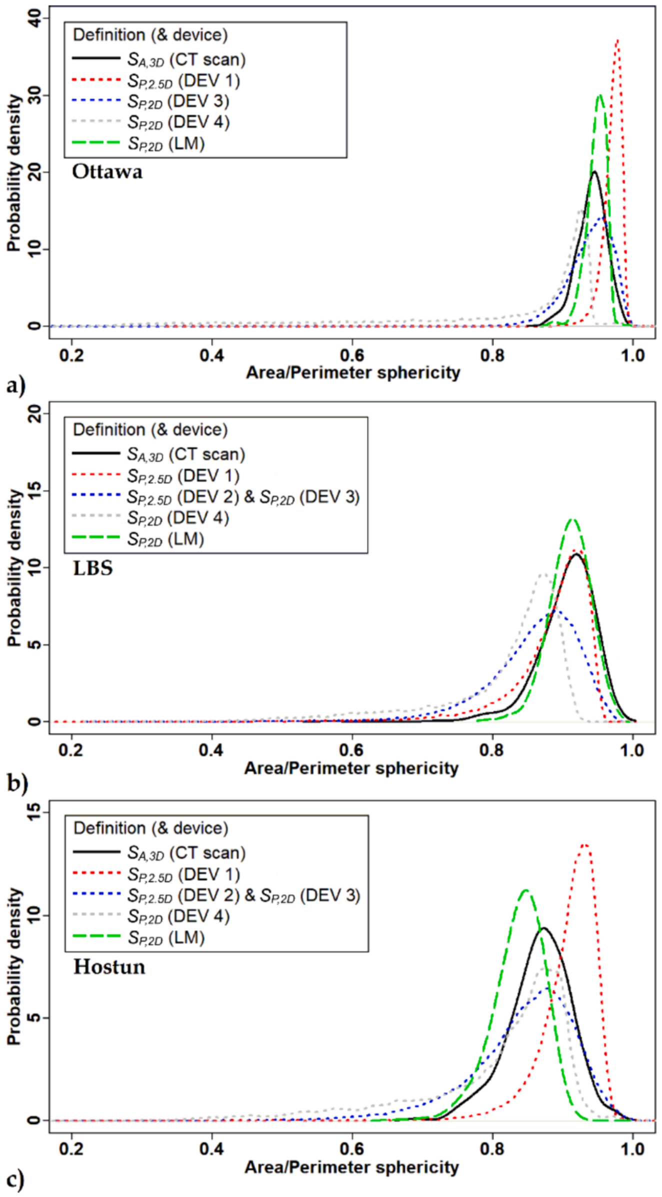

Fig. 6. PDFs of 3D true sphericity and its 2D and 2.5D proxies obtained from different devices for: (a) Ottawa; (b) LBS; and (c) Hostun.

Table 4
Hellinger distances for similarities of PDFs between 3D true sphericity and its 2D proxies from different devices.

Ottawa 20/30	$S_{A,3D}$ (CT scan)	$S_{P,2D}$ (DEV 3)	$S_{P,2.5D}$ (DEV 2)	$S_{P,2D}$ (DEV 4)	$S_{P,2D}$ (LM)
$S_{A,3D}$ (CT scan)	1	0.77	0.46	0.38	0.76
$S_{P,2D}$ (DEV 3)		1	0.52	0.44	0.58
$S_{P,2.5D}$ (DEV 1)			1	0.15	0.38
$S_{P,2D}$ (DEV 4)				1	0.26
$S_{P,2D}$ (LM)					1
LBS Frac D	$S_{A,3D}$ (CT scan)	$S_{P,2.5D}$ (DEV 2&3)*	$S_{P,2.5D}$ (DEV 1)	$S_{P,2D}$ (DEV 4)	$S_{P,2D}$ (LM)
$S_{A,3D}$ (CT scan)	1	0.61	0.78	0.43	0.85
$S_{P,2.5D}$ (DEV 2&3)*		1	0.79	0.70	0.57
$S_{P,2.5D}$ (DEV 1)			1	0.56	0.71
$S_{P,2D}$ (DEV 4)				1	0.35
$S_{P,2D}$ (LM)					1
Hostun	$S_{A,3D}$ (CT scan)	$S_{P,2.5D}$ (DEV 2&3)*	$S_{P,2.5D}$ (DEV 1)	$S_{P,2D}$ (DEV 4)	$S_{P,2D}$ (LM)
$S_{A,3D}$ (CT scan)	1	0.73	0.62	0.68	0.79
$S_{P,2D}$ (DEV 2&3)*		1	0.58	0.80	0.70
$S_{P,2.5D}$ (DEV 1)			1	0.47	0.41
$S_{P,2D}$ (DEV 4)				1	0.67
$S_{P,2D}$ (LM)					1

* Distribution of $S_{P,2.5D}$ obtained from DEV 2 was exactly the same as the distribution of $S_{P,2D}$ from DEV 3.

random projections until 100 projections. This finding is consistent with the results reported by Sandeep et al. (2023) who used randomly generated computational particle geometries termed 'particle avatars'. Second, in all cases, the deviation was smaller for maximum particle projection (i.e., higher estimation accuracy) compared to 30 random projections which is the maximum possible images that can be captured by DEV 1 and DEV 2. Notably, the number of images captured by a DIA device depends on several factors and is usually smaller than 30; as such, DEV 1 took 13 to 21 images from each particle. Third, except for very few cases, the maximum particle projection provided higher estimation accuracy when compared to 150 random projections, encouraging the use of maximum particle projection for determining $S_{P,2D}$. Finally, the more spherical the particles, the smaller would be the deviations. Indeed, the smallest deviations belonged to the class which has $S_{A,3D}$ in the range of 0.90 to 1.00. The deviations increased with increasing degree of particle elongation as $S_{A,3D}$ reduced. This trend is somewhat expected because more spherical particles would have particle projections close to a circle (hence $S_{A,2D}$ close to 1.0) regardless of the orientation of the images being captured. Accordingly, strong association between $S_{P,2D}$ and $S_{A,3D}$ is expected; in this case, the data points representing highly spherical particles would be located close to the 1:1 line (i.e., line of perfect agreement), whereas the data points representing more elongated particles would be more deviated from this line.

The relationships between $S_{A,3D}$ and $S_{P,2D}$ for four selected number of random projections (i.e., 5, 30, 100 and 150) and the maximum particle projection for all the 90 reconstructed 3D particle volumes are shown in Fig. 10. As expected and previously asserted, strong association between $S_{P,2D}$ and $S_{A,3D}$ can be found for any number of random projections with correlation coefficients (ρ) ranging from 0.92 to 0.97 and a high ρ of 0.89 for the maximum particle projection (see also Fig. 8). Specifically, the small number of particle projections, say 5, gave overestimation of $S_{A,3D}$ in all cases by up to 25 %. Increasing the number of particle projections to 30 improved the accuracy of estimation, and the amount of overestimation of $S_{A,3D}$ dropped to 15 %. The trend lines obtained for 100 and 150 random particle projections were almost the same and both of them are quite close to the correlation reported by Sandeep et al. (2023) who used a different database. However, the maximum particle projection provided a trend line that is closest to the line of perfect agreement (i.e., highest estimation accuracy); the overestimation of $S_{A,3D}$ was no more than 7.5 %. A regression analysis for this set of data returned the following expression:

$$S_{A,3D} = 1.07S_{P,2D} - 0.10; \rho = 0.89 \tag{3}$$

The results of this additional analysis suggest that the correlation be-

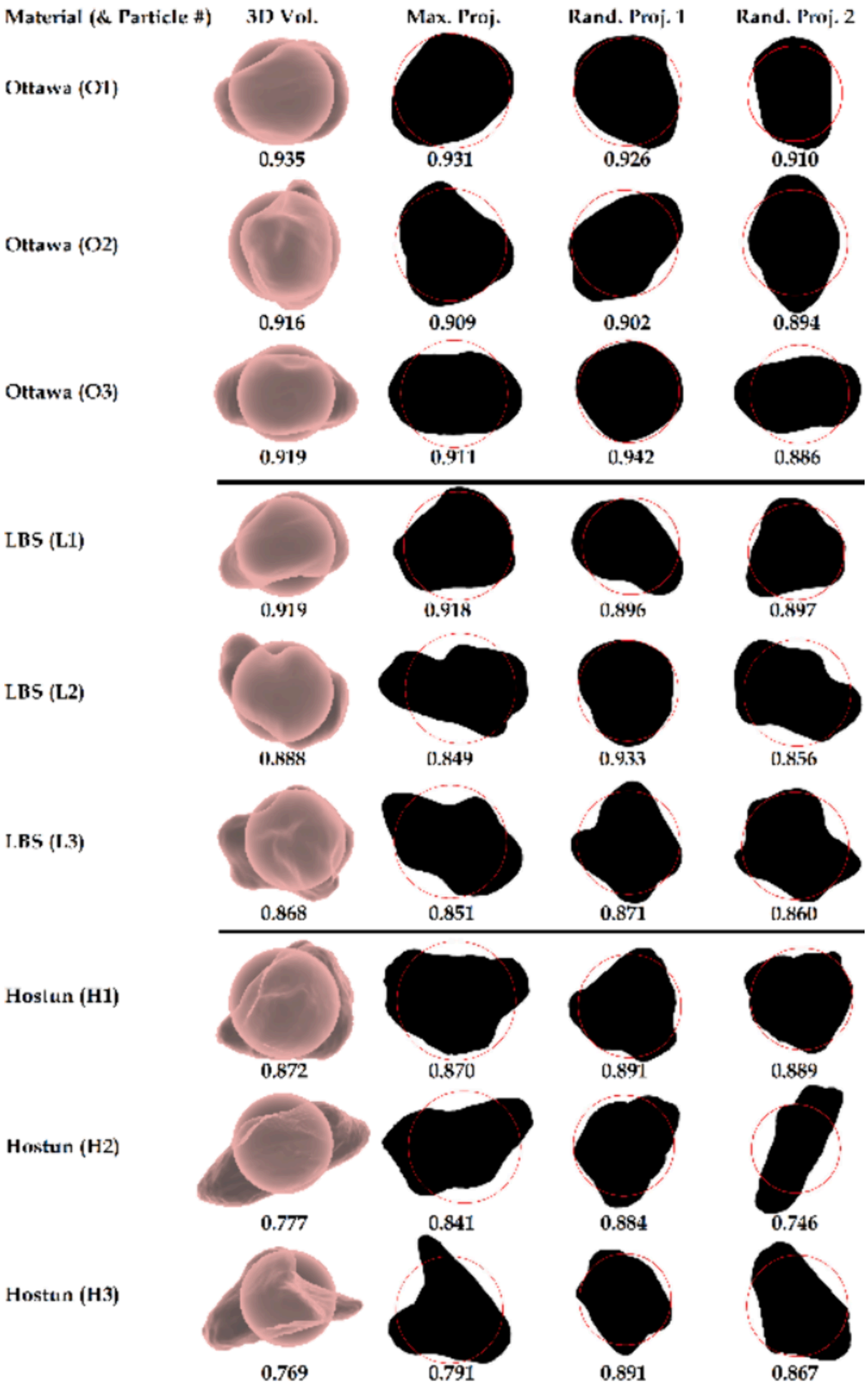

Fig. 7. Examples of computed sphericity for 3D volume reconstructions and 2D projections of the tested sands. The volume-equivalent spheres for 3D volumes and area-equivalent circles for 2D projections are given for reference.

tween $S_{A,2D}$ and $S_{A,3D}$ is high when the maximum particle projection was used for determining its 2D proxy $S_{P,2D}$. Also, overestimations of $S_{A,3D}$ are limited to 7.5 %. The priority in developing or modifying computational algorithms of 2.5D DIA devices should be given to capturing maximum particle projection and using it to determine $S_{P,2D}$. An alternative which provides somewhat less accurate estimates would be to enlarge the viewing area in the configuration of DIA devices to increase the number of images captured for each particle from up to 30 to up to 100. Owing to the particle tracking method employed in these devices (Fig. 1), the height of viewing area should be enlarged which may not be practical or incur extra cost due to the need to install more cameras.

The mean values of sphericity obtained from the different devices and percentage deviations from the µCT results are summarized in Fig. 11. The APDs obtained for LM are remarkably small (0.7 % – 1.9 %). DEV 4 has the worst performance as its deviations were as large as 14.2 %. DEV 1 and DEV 3 have small to moderate deviations in the range of 2.6 % to 6.9 %. It is surprising that DEV 1, which cannot provide acceptable estimates of mean aspect ratio for LBS sand, is capable of doing so for a finer descriptor (i.e., sphericity) in the same sand.

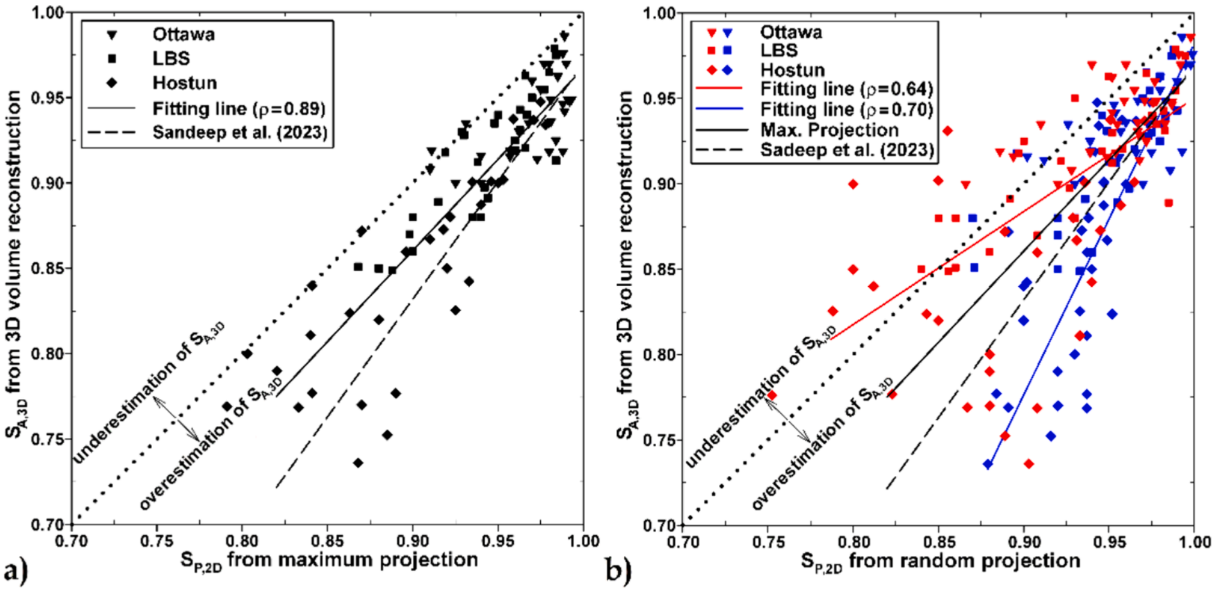

Fig. 8. Relationship between $S_{A,3D}$ and $S_{P,2D}$ for: (a) maximum particle projections, and (b) randomly-oriented projections (Notes: blue and red colors indicate $S_{P,2D}$ values obtained for two different random projections). (For interpretation of the references to colour in this figure legend, the reader is referred to the web version of this article.)

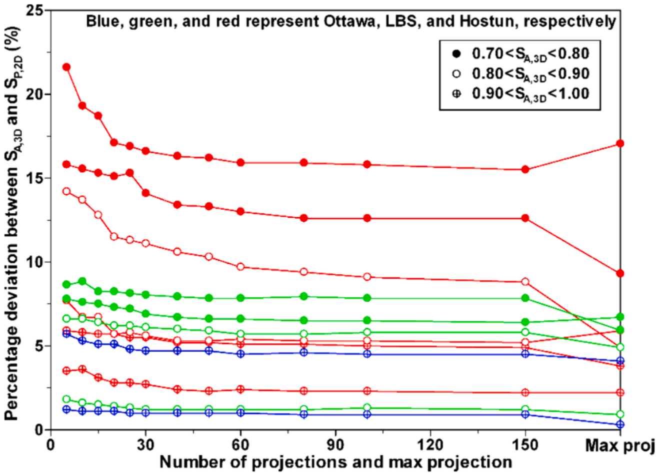

Fig. 9. Absolute percentage deviation of $S_{P,2D}$ from $S_{A,3D}$ for different numbers of random projections and the maximum particle projection for two typical particles from each tested sand (Note: none of the Ottawa particles randomly selected for this analysis had $S_{A,3D} \leq 0.8$; thus no Ottawa particles belong to the class with $0.7 < S_{A,3D} < 0.8$ in the figure).

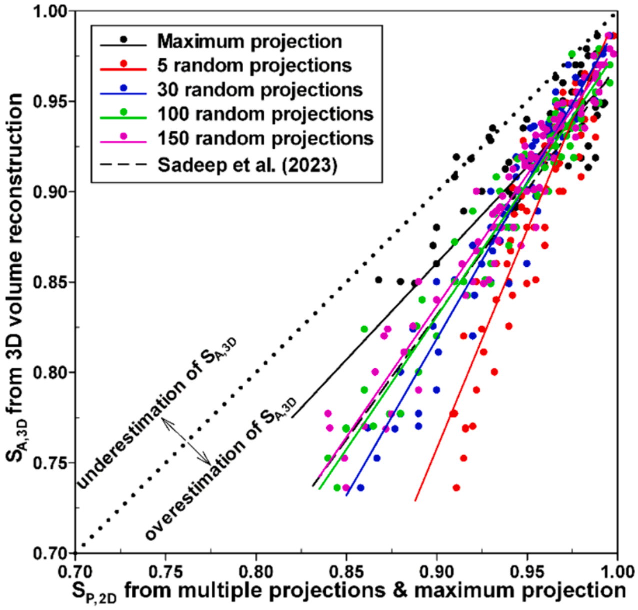

Fig. 10. Relationship between $S_{A,2D}$ and $S_{A,3D}$ for selected number of random projections (5, 30, 100 and 150) and maximum particle projection.

3.2.3. Convexity

The PDFs of convexity (C_x) obtained from different devices and the corresponding HD values are summarized in Fig. 12 and Table 5, respectively. DEV 1 and DEV 3 provided quite different distributions, with relatively low HD values of 0.25 and 0.24, respectively. The PDFs obtained by LM have moderate to high similarities (HD range: 0.68–0.83). DEV 4 returned the PDFs for the Ottawa and Hostun that are somewhat comparable with the μCT and LM results but failed to provide an acceptable PDF in the case of LBS (with a low PDF similarity of only 29 %; Table 5).

Notably, convexity, similar to sphericity, is a measure of particle compactness or its proximity to a sphere or circle in 3D and 2D, respectively; indeed, previous studies have found a strong correlation between convexity and sphericity (Fonseca et al. 2012; Rorato et al. 2019). Thus, the results of the extra analyses for the influence of particle projection on sphericity determination in the previous section may be applied here too. As such, particle projection might be the reason for the remarkably high differences between the PDFs obtained from μCT and DIA. However, the differences are more pronounced in the case of convexity. Therefore, other factor(s) that more seriously affect(s) the determination of C_x may exist. Inadequacy of camera resolution could be a reason that affected some or all of the DIA devices evaluated. In fact, convexity is a very fine descriptor that, similar to the evaluation of particle roundness, requires the evaluation of curvilinearities of particle perimeters (Sun et al. 2019) and thus demands a high image resolution among the descriptors of first- and second-order properties. DEV 1, which has the lowest camera resolution among the three devices evaluated (i.e., 15 μm/pixel compared to 1–7 for DEV 2 to 4), was affected by the camera resolution because it provided quite different PDFs from the

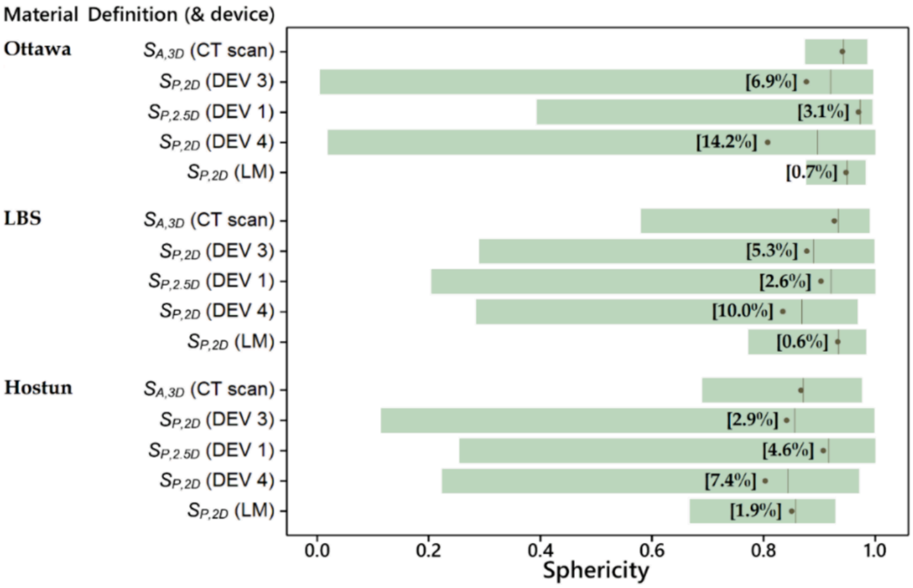

Fig. 11. Box plot of 3D true sphericity and its 2D and 2.5D proxies obtained from different devices. Note: points and lines indicate mean and median values, respectively, and the values in the brackets are APD.

μCT results. While the camera resolution of DEV 3 (1 μm/pixel; Table 1) is much higher, an extra factor that affected the performance of DEV 3 is the inconsistent definition used to determine C_x (i.e., $\sqrt{A_{2D}/A_c}$ versus A_{2D}/A_c; Table 2), returning high values of C_x regardless of the angularity of the particles. While the use of randomly-oriented projections instead of maximum projections affected the performance of all the DIA devices, factors such as inadequacy of the camera resolution (i.e., DEV 1) and inconsistency in the definition of convexity (i.e., DEV 3) affected only some of them and amplified the difference between μCT and DIA results.

Fig. 13 shows the mean values of convexity obtained from the different devices. Referring to percentage deviations from μCT results it can be seen that quite small APDs ranging from 0.4 % to 1.2 % were obtained for LM. All the DIA devices have small to moderate deviations with APDs in the range of 2.1 % to 8.8 %. Yet, their PDFs are quite different. This is a good example demonstrating that morphological descriptors with similar mean values may have quite different probability distributions.

3.3. Second-order morphological properties

The PDFs of roundness obtained from different devices and the corresponding HD values are summarized in Fig. 14 and Table 6, respectively. Except for DEV 1 when applied to Ottawa, all DIA devices provided PDFs quite different from the μCT result. Note that DEV 2 and DEV 3 use automatic particle threshold search to identify overall particle shapes (i.e., edges and corners) and employ a computational algorithm for roundness determination that requires smoothing of the particle surfaces (i.e. removing particle roughness). This process involves identifying particle's corners and fitting circles to them to determine $R_{ci,2D}$, $R_{ins,2D}$ and N (Table 1), which all depend on proper smoothing of the particle surfaces. DEV 3 provided a PDF for Ottawa that was different from the μCT result and overestimated the roundness in most cases. Notably, Ottawa sand has rounded particles with quite smoothed surfaces so no smoothing of the particle surfaces or only a small amount of smoothing is needed. Based on the analyzed results, DEV 3 failed to detect the exact values of either $R_{ci,2D}$, $R_{ins,2D}$, and N or all of them, resulting in overestimation of roundness. For LBS and Hostun, DEV 2 and DEV 3 provided PDFs that were quite different from the μCT result (i.e. 28 % to 45 % PDF similarity), and significantly underestimated the roundness. Given these two devices have high camera resolutions (i.e., up to 1 μm/pixel; Table 2), the reason for the underestimation may be related to the determination algorithm adopted in their built-in software, by which no proper smoothing of the particle surfaces was performed and all the asperities on a particle surface were considered as particle corners, leading to unrealistically small values of roundness. Indeed, both DEV 2 and DEV 3 registered values of R close to zero (e.g., 0.002 and 0.005), which is possible only when most of the asperities on a particle surface were considered as particle corners even though they belonged to a lower scale (i.e., micro-scale surface roughness). Referring to the raw data, DEV 2 and DEV 3 provided $R_{2.5D}$ and R_{2D} values as small as 0.00005 and 0.006, respectively. Removal of particle roughness has been shown to be a prerequisite for proper determination of R_{2D} if Wadell's definition is used (Zheng and Hryciw 2015). DEV 1 provided a PDF for Ottawa that is fairly similar to the one obtained from the μCT (i.e., 56 % PDF similarity). However, when applied to sands with more angular particles that have smaller particle sizes (i.e., LBS and Hostun), DEV 1 significantly overestimated the roundness and provided remarkably different PDFs, having only 4 % to 6 % PDF similarity. Notably, DEV 1 employs a rather different algorithm for roundness determination, compared to DEV 2 and DEV 3. DEV 1 uses an adjustable threshold for detecting the exact particle's edges and corners. This manual method may also apply smoothing of the particle surfaces at the same time of detecting the overall shape (i.e., edges and corners) of each particle. With relatively low camera resolution of 15 μm/pixel, DEV 1 was able to capture fairly accurate overall particle shapes for Ottawa that is a sand with coarse to very coarse particles. However, this resolution was insufficient to capture the accurate overall particle shapes for LBS and Hostun that are sands with fine to medium fine particles. Indeed, as mentioned in the previous section, the poor performance of this particular device in estimating particle convexity was partly due to the inadequacy of its camera resolution.

The PDFs obtained by LM have larger HD values ranged between 0.67 and 0.77 for the three tested sands and thus are relatively closer to the μCT results than using DIA. Yet, the LM showed the lowest capability in estimating R_{3D} compared with the other morphological descriptors (i.e., HDs as high as 0.77 for R compared to 0.96, 0.85, and 0.83 for $AR_{W/L}$, S, and C_x, respectively). The fundamental difference between the methods of determining the particle roundness using 3D volumes and 2D projections could be the major cause for this performance drop. Corner spheres in a 3D particle are always smaller than or equal to the corner circles in their 2D projection counterparts (Li et al. 2023). Yet, projection direction may also affect the 2D roundness estimation.

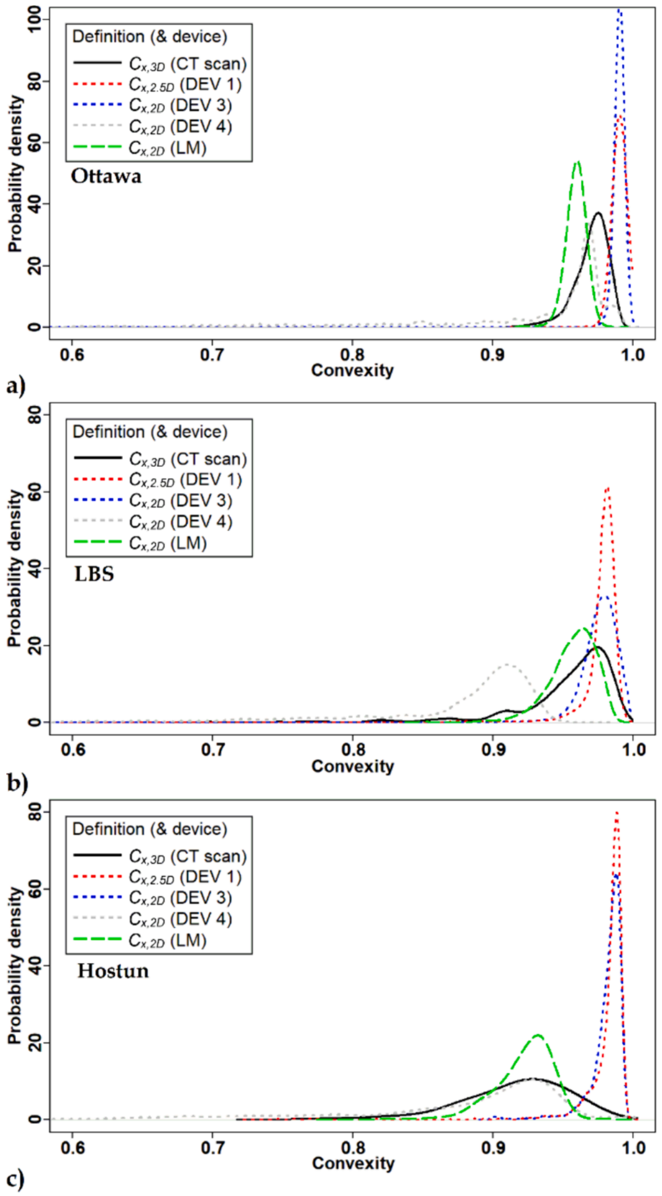

Fig. 12. PDFs of 3D convexity and its 2D and 2.5D proxies from different devices for: (a) Ottawa; (b) LBS; and (c) Hostun.

To elaborate more on the effects of particle projection on the R_{2D} determination, analyses similar to that conducted for sphericity were carried out using the same μCT reconstructed 3D volumes of the 90 particles used before. Fig. 15(a) and 15(b) correlate R_{3D} with R_{2D} obtained by maximum projection and that with two randomly-oriented projections, respectively. First, similar to the trend observed for sphericity, R_{2D} from maximum projection is more strongly correlated with R_{3D} [$\rho = 0.83$ in Fig. 15(a)] than R_{2D} from any of the two random projections [$\rho = 0.74$ and 0.76 in Fig. 15(b)] but the difference between the two cases is not as pronounced as that observed for sphericity (i.e., $\rho =$ 0.89 versus 0.64 and 0.70 in the preceding section). Therefore, compared with random projections, the maximum projections can somewhat better represent their 3D counterparts when determining particle roundness. Yet, a similar trend was obtained between R_{3D} and R_{2D} regardless of the method of capturing projection. Based on the results, similar performance should be expected for the two devices that work based on randomly-oriented projections (DEV 3) and maximum projections (LM), but the data presented in Fig. 14 and Table 6 suggested otherwise; low PDF similarities were found between DEV 3 and LM, with HD values ranged between 0.44 and 0.57. Second, the trends obtained between R_{3D} and R_{2D} indicate a tendency for the underestimation of R_{3D} for angular particles (i.e., Hostun), while slightly overestimating the R_{3D} values for rounded particles (i.e., Ottawa). The observation of tendencies for underestimating of R_{3D} for angular particles and overestimating of R_{3D} for rounded particles agrees with the PDFs obtained using the LM for these two test materials. Indeed, compared with the PDF of R_{3D} obtained from the μCT, the PDFs of R_{2D} obtained for Hostun and Ottawa were slightly shifted to the left and right, respectively. The same applies to the PDF obtained using DEV 1 for the Ottawa but not for the other two sands because of the lack of camera resolution for the determination of R_{2D} for them.

Table 5
Hellinger distances for similarities of PDFs between 3D convexity and its 2D proxies from different devices.

Ottawa 20/30	$C_{x,3D}$ (CT scan)	$C_{x,2D}$ (DEV 3)	$C_{x,2.5D}$ (DEV 1)	$C_{x,2D}$ (DEV 4)	$C_{x,2D}$ (LM)
$C_{x,3D}$ (CT scan)	1	0.25	0.32	0.57	0.68
$C_{x,2D}$ (DEV 3)		1	0.86	0.18	0.05
$C_{x,2.5D}$ (DEV 1)			1	0.21	0.07
$C_{x,2D}$ (DEV 4)				1	0.49
$C_{x,2D}$ (LM)					1
LBS Frac D	$C_{x,3D}$ (CT scan)	$C_{x,2D}$ (DEV 3)	$C_{x,2.5D}$ (DEV 1)	$C_{x,2D}$ (DEV 4)	$C_{x,2D}$ (LM)
$C_{x,3D}$ (CT scan)	1	0.65	0.46	0.29	0.83
$C_{x,2D}$ (DEV 3)		1	0.63	0.08	0.61
$C_{x,2.5D}$ (DEV 1)			1	0.07	0.37
$C_{x,2D}$ (DEV 4)				1	0.17
$C_{x,2D}$ (LM)					1
Hostun	$C_{x,3D}$ (CT scan)	$C_{x,2D}$ (DEV 3)	$C_{x,2.5D}$ (DEV 1)	$C_{x,2D}$ (DEV 4)	$C_{x,2D}$ (LM)
$C_{x,3D}$ (CT scan)	1	0.24	0.25	0.72	0.74
$C_{x,2D}$ (DEV 3)		1	0.89	0.16	0.13
$C_{x,2.5D}$ (DEV 1)			1	0.17	0.13
$C_{x,2D}$ (DEV 4)				1	0.62
$C_{x,2D}$ (LM)					1

Similar to the previous sections, a theoretical computation was performed using the 90 randomly selected 3D particle volumes reconstructed by μCT to investigate the effect of number of particle projections on the computation accuracy of roundness. The same number of random projections (i.e., 5, 10, 15, 20, 25, 30, 40, 50, 60, 80, 100, and 150) was used and mean value of 2D roundness (R_{2D}) was computed for

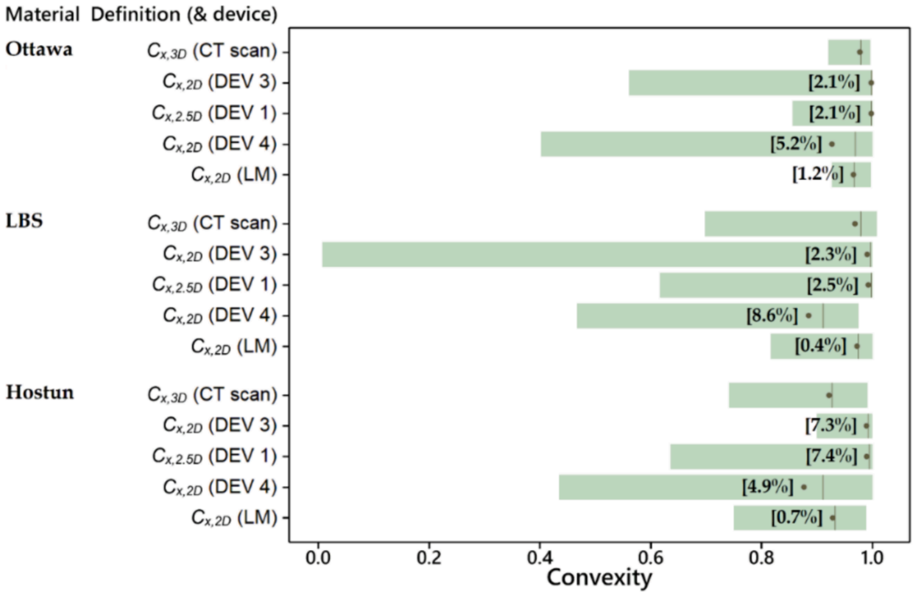

Fig. 13. Box plot of 3D convexity and its 2D and 2.5D proxies obtained from different devices (Notes: points and lines indicate mean and median values; values in brackets indicate APD with reference to μCT result).

these random particle projections. Fig. 16 shows the absolution percentage deviation of R_{2D} from 3D roundness (R_{3D}) for different numbers of random projections and the maximum particle projection. Notably, negative and positive deviations (i.e. over- and underestimation of R_{3D}, respectively) were obtained so absolute percentage deviations are presented in the figure. The roundness data was categorized into three classes of particle angularity, namely $0.35 < R_{3D} < 0.50$, $0.50 < R_{3D} < 0.65$ and $0.65 < R_{3D} < 0.80$. Only two typical particles from each tested sand were presented for brevity. First, similar to the case of sphericity, the deviation always reduced with increasing number of random projections from 5 to 100 but for larger number of projections (i.e. 150) negligible change in the deviation was found in most cases, though the deviation in some cases continued to drop. In other words, the accuracy of estimating R_{3D} increased with increasing number of random projections until 100 projections and even until 150 projections, indicating that accurate estimation of roundness using 2D random projections may require larger number of random projections compared to sphericity. Second, in almost half of the cases, the deviation resulting from the use of maximum particle projection was larger (i.e., lower estimation accuracy) compared to 30 random projections, while in the other half, the maximum particle projection resulted in smaller deviations. Third, in most cases, the maximum particle projection provided a slightly lower estimation accuracy when compared to 150 random projections, while in a few cases, it provided higher accuracy. This finding means that unlike the estimation of sphericity, the use of maximum particle projection may or may not provide improved estimation of R when compared to using multiple random projections. Finally, no clear trend between degree of particle angularity and accuracy of roundness estimation can be identified. For example, one of the most rounded particles of Ottawa with R_{3D}~0.80 has the largest deviation range (27 % to 36 %) for particle projections ranged from 5 to 150. On the contrary, a very angular particle of Hostun with R_{3D}~0.45 has much smaller deviations in the range of 1 % to 10 % for particle projections ranged from 5 to 150. Moreover, unlike sphericity, estimating R_{3D} using either maximum particle projection or different number of particle projections (e.g., 50, 100, 150) could result in either under- or overestimation. The reason is the fundamental difference between the determination of R_{3D} and R_{2D} where spheres are fitted to corners and ridges of a 3D particle to compute R_{3D} of a certain particle, while circles are fitted to corners and two-dimensional ridges or bumps of its 2D projection to compute R_{2D}. Accordingly, the association between R_{2D} and R_{3D} was somewhat scattered and may be not as strong as that observed between $S_{P,2D}$ and $S_{A,3D}$ (Fig. 10).

The relationships between R_{2D} and R_{3D} for four selected number of random projections (i.e., 5, 30, 100 and 150) and the maximum particle projection for all the 90 reconstructed 3D particle volumes are shown in Fig. 17. As previously asserted, the data of roundness was much scattered compared to the sphericity data. Accordingly, correlations between R_{2D} and R_{3D} for different numbers of random projections were weak to moderate with ρ ranging from 0.57 to 0.78, while the correlation for the maximum particle projection was moderately high with ρ of 0.83 (Fig. 15). Specifically, the small number of particle projections, say 5, showed the weakest correlation (i.e. $\rho = 0.57$) and provided over- and underestimation of R_{3D} by 60 % and 45 %, respectively. The accuracy of estimation and the correlation between R_{2D} and R_{3D} were improved by increasing the number of particle projections from 5 to 30 such that the over- and underestimation of R_{3D} were less than 35 % and 25 %, respectively. The trend line obtained for 30 random projections was close to those obtained for 100 and 150 random projections, but because the latter was less deviated from the line of perfect agreement, the estimation accuracy for the 100 and 150 random projections was higher. The trend line obtained for the maximum particle projection was slightly deviated from those obtained for 30, 100 and 150 random projections. The over- and underestimations resulting from the use of maximum particle projection were limited to 25 % and 35 %, respectively, indicating similar accuracy to using 30, 100 and 150 random particle

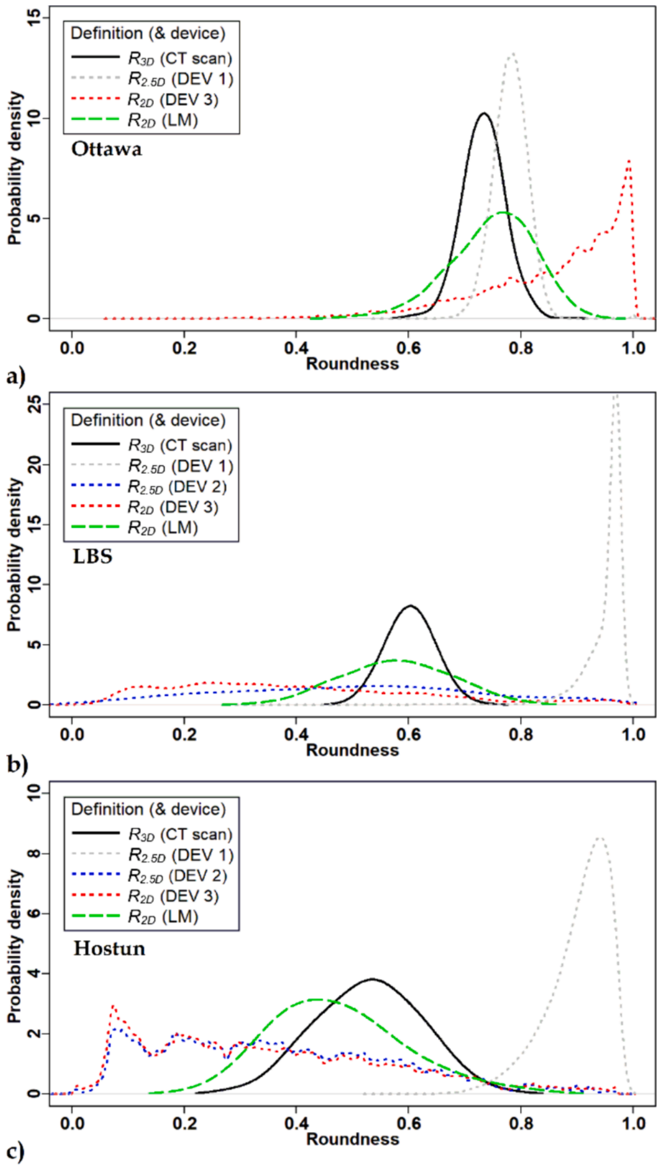

Fig. 14. PDFs of 3D roundness and its 2D and 2.5D proxies from different devices for: (a) Ottawa; (b) LBS; and (c) Hostun.

projections. A regression analysis for this set of data returned the following expression:

$$R_{3D} = 1.07R_{2D} - 0.10; \rho = 0.83 \tag{4}$$

The additional analysis suggests that using both maximum particle projection and average from a large number of random projections such as 30, 100 and 150 would result in the same accuracy when estimating R_{3D} through its 2D proxy. The correlation between R_{2D} and R_{3D} was moderately high and over- and underestimation of R_{3D} as large as 35 % can be expected when using its 2D proxy, irrespective to the use of maximum particle projections or large random particle projections of even up to 150. To improve the estimation accuracy of roundness in 2.5D DIA devices, it may be more effective to modify their computational algorithms to capture the maximum particle projection of the particles, when compared to the effort needed to increase the number of images captured for each particle to up to 100 or 150.

The box plot of roundness values from different devices along with the corresponding APDs from the µCT results is shown in Fig. 18. The APDs obtained for LM were either very small (2.1 % and 4.0 % in Ottawa and LBS, respectively) or acceptably moderate (10.3 % in Hostun). On the other hand, except for DEV 1 when applied to Ottawa, the APDs for DIA devices were very large to extremely large as they ranged from 16.6 % to 70.7 %. Thus, none of the DIA devices performed acceptably in terms of having small APD. It should be noted that mean values of Wadell roundness *R* have been mainly used in angularity classification through the classification system proposed by Powers (1953). Using the mean values of *R* from µCT as reference values along with this classification system, the *CSR* for DEV 1, 2, 3 and LM was 33 %, 66 %, 33 % and 100 %, respectively.

Table 6
Hellinger distances for similarities of PDFs between 3D roundness and its 2D proxies from different devices.

Ottawa 20/30	R_{3D} (CT scan)	R_{2D} (DEV 3)	$R_{2.5D}$ (DEV 1)	R_{2D} (LM)	
R_{3D} (CT scan)	1	0.31	0.56	0.70	
R_{2D} (DEV 3)		1	0.32	0.44	
$R_{2.5D}$ (DEV 1)			1	0.58	
R_{2D} (LM)				1	
LBS Frac D	R_{3D} (CT scan)	$R_{2.5D}$ (DEV 2)	R_{2D} (DEV 3)	$R_{2.5D}$ (DEV 1)	R_{2D} (LM)
R_{3D} (CT scan)	1	0.37	0.28	0.05	0.67
$R_{2.5D}$ (DEV 2)		1	0.82	0.18	0.57
R_{2D} (DEV 3)			1	0.15	0.44
$R_{2.5D}$ (DEV 1)				1	0.07
R_{2D} (LM)					1
Hostun	R_{3D} (CT scan)	$R_{2.5D}$ (DEV 2)	R_{2D} (DEV 3)	$R_{2.5D}$ (DEV 1)	R_{2D} (LM)
R_{3D} (CT scan)	1	0.49	0.46	0.04	0.77
$R_{2.5D}$ (DEV 2)		1	0.94	0.11	0.60
R_{2D} (DEV 3)			1	0.13	0.57
$R_{2.5D}$ (DEV 1)				1	0.07
R_{2D} (LM)					1

4. Summary and conclusions

Systematic evaluation of the efficacy of morphology characterization using four DIA devices (two 2D devices and two 2.5D devices) and an LM in comparison with the µCT results was made by selecting statistical representative samples for all the imaging techniques evaluated. Test results of three standard sands that covered a wide range of particle form and angularity were used in the assessment. A relative entropy measure (i.e., Hellinger distance, HD) and absolute percentage deviation were used to quantitatively compare the similarity of PDFs and mean values of morphological descriptors obtained from different imaging techniques in comparison with the µCT results. The following conclusions may be drawn based on the analyses conducted:

- Because of the requirement of low image resolution and its straightforward computation, reliable PDFs and mean values for width-to-length aspect ratio can be obtained from most of the imaging techniques, irrespective of the static or dynamic nature and 2D or 3D imaging. However, the thickness-to-length aspect ratio can be reliably obtained only by µCT.
- When used for subangular and angular particles, DIA devices provided probability distributions for roundness and convexity that are completely different from the µCT results. The PDF similarity was only 4 %–6% and 24 %–25 % for roundness and convexity, respectively.

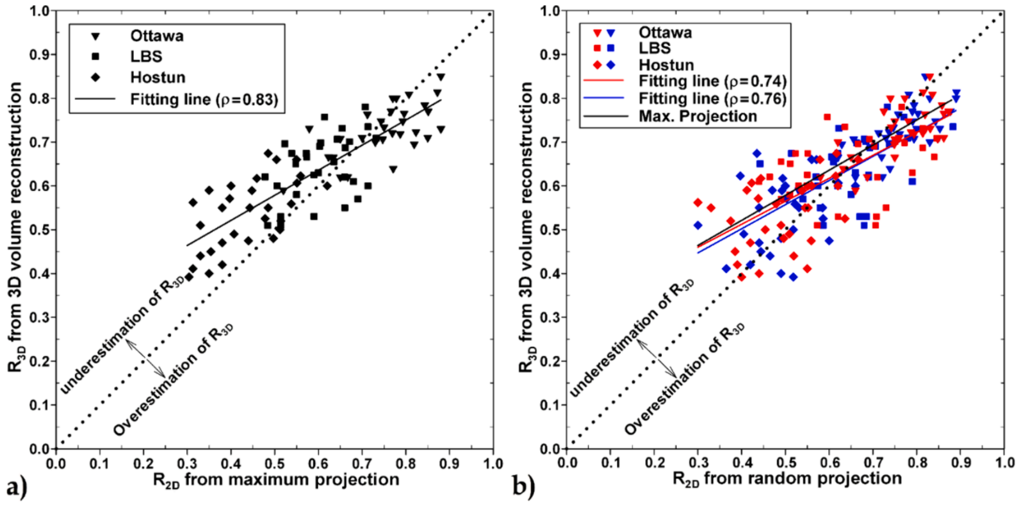

Fig. 15. Relationship between R_{3D} and R_{2D} for: (a) maximum particle projections, and (b) randomly-oriented projections (Notes: blue and red colors indicate R_{2D} values obtained for two different random projections). (For interpretation of the references to colour in this figure legend, the reader is referred to the web version of this article.)

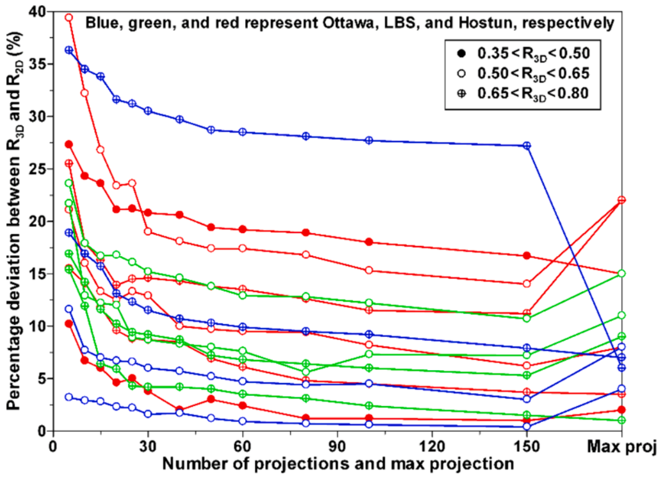

Fig. 16. Absolute percentage deviation between 2D and 3D roundness for different numbers of random projections and the maximum particle projection for two typical particles from each tested sand (Note: none of the Ottawa and LBS particles randomly selected for this analysis had $R_{3D} \leq 0.65$; thus no Ottawa and LBS particles belong to the class with $0.35 < R_{3D} < 0.50$ and $0.50 < R_{3D} < 0.65$).

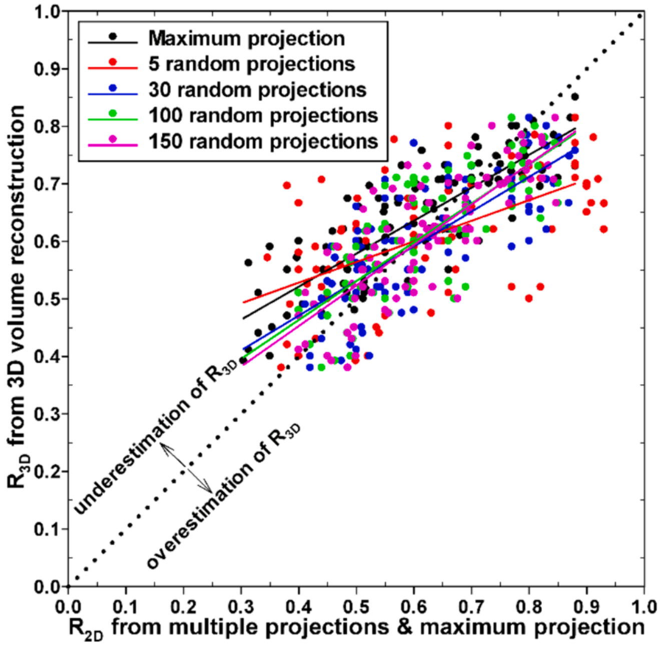

Fig. 17. Relationship between R_{2D} and R_{3D} for selected number of random projections (5, 30, 100 and 150) as well as maximum particle projection.

- Most DIA devices provided mean values of roundness quite different from μCT results. The absolute percentage deviations from the μCT results were very large to extremely large, ranging from 17 % to 71 %, resulting in rather different angularity classifications.
- The 2D perimeter sphericity (S_P) obtained from maximum projections better represents its 3D counterpart, when compared with values obtained from randomly-oriented projections even if average from multiple random projections in the order of 100 is obtained. The same does not apply to 2D and 3D roundness since both maximum projection and average from a large number of random projections provide the same accuracy when estimating the roundness. Thus, static imaging methods such as LM that work based on maximum projections can provide PDFs and mean values closer to μCT, when compared to DIA.
- The determination of S_P in the current 2.5D DIA devices may be improved by modifying their device configuration and/or computational algorithm so that S_P can be determined based on either the captured image with the largest area or averaging from multiple random projections in the order of 100.

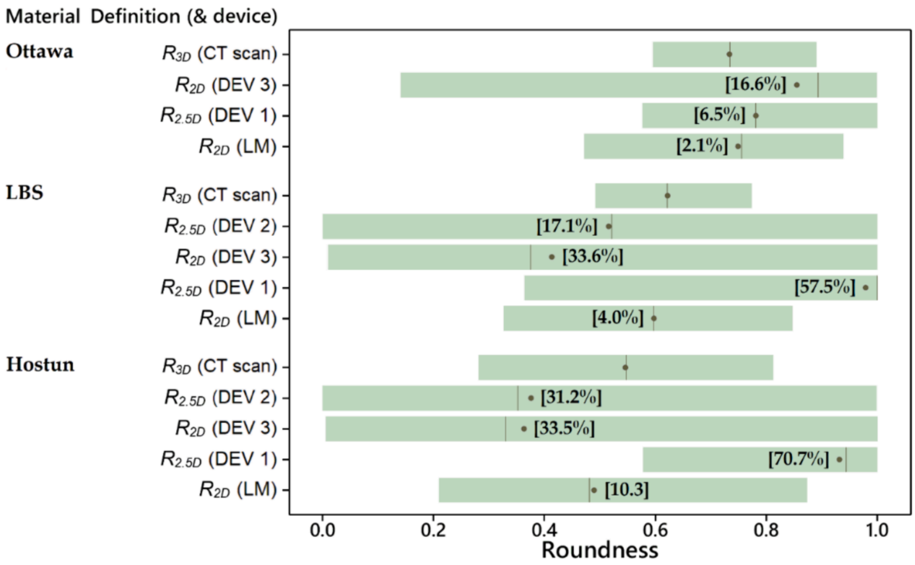

Fig. 18. Box plot of 3D roundness and its 2D and 2.5D proxies obtained from different devices (Notes: points and lines indicate mean and median values; values in brackets indicate APD with reference to μCT result).

- Among all the imaging methods and devices evaluated, the results (PDFs and mean values) derived from the LM have acceptably high similarities to the μCT results for all the morphological descriptors and sands considered in this study.

Based on the observations, it may be concluded that most DIA devices can be reliably used for coarse descriptors such as width-to-length aspect ratio in sands of a wide particle size ranging from very fine to coarse, while some devices require improvement in their camera resolution to be applied to fine sands. However, application of DIA devices to determine very fine to medium fine descriptors in fine to medium fine sands might require significant improvement in their camera resolution and especially computational algorithms in their built-in software.

A practical implication of this study is that, while the determination of 3D morphological descriptors for sand particles is a challenging task due to the computational workload required, through the easy-to-follow procedure developed in this study and using an LM that is readily available in most cases, mean values and PDFs of descriptors acceptably similar to μCT results can be obtained, resulting in a significant saving of time and effort while obtaining the same class of particle shape and angularity. Accordingly, images and PDFs from LM can be used for inclusion in 3D printing process and DEM modeling to fabricate 2D analog granular assemblies that can capture the morphological effects of real soil particles without having to conduct 3D scanning and DEM simulations.

Funding

This work was supported by the General Research Fund #C6006-20G and #16207521 funded by the Hong Kong Research Grants Council . The last author would like to acknowledge the support of the Royal Society via the International Exchanges Cost Share with the NSFC (grant no. IEC\NSFC\223020).

CRediT authorship contribution statement

Karim Kootahi: Writing – original draft, Visualization, Software, Methodology, Investigation, Formal analysis, Conceptualization. **Anthony Kwan Leung:** Writing – review & editing, Supervision, Project administration, Methodology, Funding acquisition, Conceptualization. **Zhenliang Jiang:** Writing – review & editing, Investigation, Data curation. **Jianbin Liu:** Writing – review & editing, Investigation, Data curation. **Rui Qi:** Resources, Investigation. **Sérgio D.N. Lourenço:** Writing – review & editing, Resources. **Zhengshou Lai:** Writing – review & editing, Software. **Zhiwei Gao:** Writing – review & editing, Resources.

Declaration of competing interest

The authors declare that they have no known competing financial interests or personal relationships that could have appeared to influence the work reported in this paper.

Data availability

Data will be made available on request.

Appendix A

The relative entropy-based algorithm developed by Kootahi et al. (2023b) can be used to find the RSS required for capturing the underlying PDFs of any morphological descriptor of sands. The algorithm involves (1) collecting a population or entire sample of size 1500 or more for the morphological descriptor of interest such as $S_{A,3D}$, R_{3D} or $S_{P,2D}$; (2) taking two random samples of increased size from the entire sample (e.g., $n_i = 10$ & $n_{i+1} = 50$) and finding their underlying PDFs using KDE; (3) obtaining the PDF similarity for the two PDFs using Hellinger distance [HD; Eq. (1)]; (4) repeating this process for 1000 bootstrap samples and obtaining an average HD ($\overline{D}_{\mathrm{H,avg}}$); and (5) consecutively increasing the size of random samples in an arithmetic manner (e.g., $n_{i+1} = 50$ & $n_{i+2} = 90$; $n_{i+2} = 90$ & $n_{i+3} = 130$) until observing a plateau in the PDF similarity curve (curve of n versus $\overline{D}_{\mathrm{H,avg}}$), which is computationally detected through reaching the threshold gradient of $\beta_{\mathrm{thresh}} = 1 \times 10^{-4}$ in the PDF similarity curve. This algorithm was applied to 3D sphericity ($S_{A,3D}$) data of two sands Hostun and Caicos which were reported by Rorato et al. (2019). Rorato et al. (2019) analyzed the CT images for a large number of particles of the two sands (>110,000 altogether) and provided the distribution of $S_{A,3D}$ for the two sands. After digitizing the distributions of $S_{A,3D}$ and reproducing the raw data for the two sands (47,970 and 63,815 individual $S_{A,3D}$ values for Hostun and Caicos, respectively), the algorithm proposed by Kootahi et al. (2023b) was applied; the sampling started from an initial size of 5 and arithmetically increased by 75. The result of the algorithm application and its verification are shown in Figs. A1(a) and A1(b), respectively. It may be seen from Fig. A1(a) that PDF similarity curves of $S_{A,3D}$ for Hostun and Caicos sands require sample sizes of 500 and 592, respectively, to reach the respective plateaus, and thus the RSS for Hostun and Caicos sands is 500 and 592, respectively. The verification of the results for the two sands was obtained by taking 1,000 random samples of a size equal to the obtained RSS and using Eq. (1) to quantify their PDF similarity with the respective entire samples (i.e., 47,970 and 63,815 for Hostun and Caicos, respectively). From Fig. A1(b), quite large values of $\overline{D}_{\mathrm{H,avg}}$ were found for the PDF similarity between the obtained RSS and the respective entire sample for both sands ($\overline{D}_{\mathrm{H,avg}} = 0.96$ for Hostun and $\overline{D}_{\mathrm{H,avg}} = 0.95$ for Caicos), indicating that the representative number of particles had been obtained.

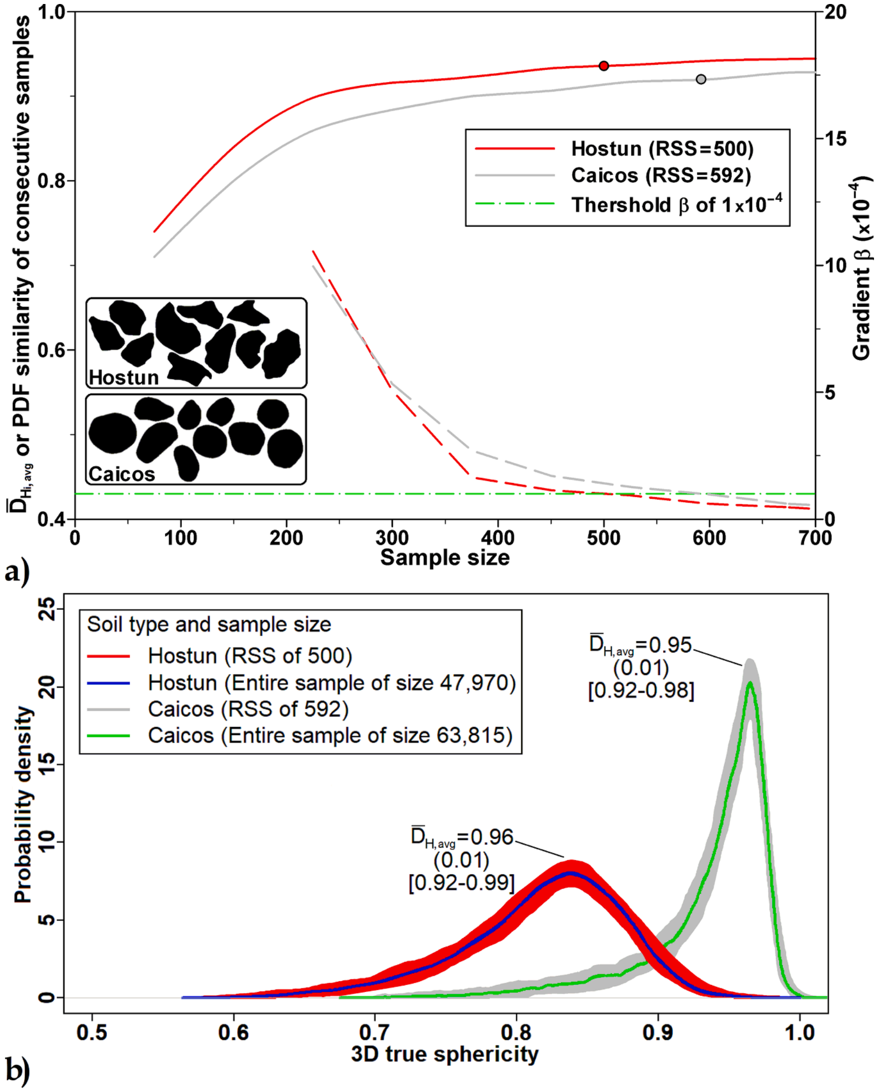

Fig. A1. Results of applying the relative entropy-based algorithm to μCT data of Hostun and Caicos sands; (a) PDF similarity curve and obtained RSS for 3D true sphericity of Hostun and Caicos sands (Notes: circles on the PDF similarity curves show RSS; solid and dashed lines show $\overline{D}_{\mathrm{H,avg}}$ and gradient β versus sample size, respectively); (b) Plots of KDEs for verification of the RSS values obtained for the two sands along with calculated values of average Hellinger distances ($\overline{D}_{\mathrm{H,avg}}$) for 1000 verification samples [Notes: SD and range of Hellinger distances are shown in parentheses and brackets, respectively; Example binary images of the two sands were obtained by analyzing a slice of 3D CT image from Rorato et al. 2019]

References

Adamidis, O., Alber, S., Anastasopoulos, I., 2020. Assessment of three-dimensional printing of granular media for geotechnical applications. Geotech Testing J 43 (3), 20180259.

Altuhafi, F., O'Sullivan, C., Cavarretta, I., 2013. Analysis of an image-based method to quantify the size and shape of sand particles. J. Geotech. Geoenviron. Eng. 139 (8), 1290–1307.

Cho, G.-C., Dodds, J., Santamarina, J.C., 2006. Particle shape effects on packing density, stiffness, and strength: natural and crushed sands. J. Geotech. Geoenviron. Eng. 132 (5), 591–602.

Cox, M.R., Budhu, M., 2008. A practical approach to grain shape quantification. Eng. Geol. 96 (1–2), 1–16.

Fonseca, J., O'Sullivan, C., Coop, M.R., Lee, P.D., 2012. Non-invasive characterization of particle morphology of natural sands. Soils Found. 52 (4), 712–722.

Garboczi, E.J., Bullard, J.W., 2017. 3D analytical mathematical models of random star-shape particles via a combination of X-ray computed microtomography and spherical harmonic analysis. Adv. Powder Technol. 28 (2), 325–339.

Gardner, P., Lord, C., Barthorpe, R.J., 2019. A Unifying Framework for Probabilistic Validation Metrics. J Verif Valid Uncert 4 (3), 031005.

Gokhale, D.V., Kullback, S., 1978. The information in contingency tables. Marcel Dekker Inc, New York.

Kong, D., Fonseca, J., 2018. Quantification of the morphology of shelly carbonate sands using 3D images. Géotechnique 68 (3), 249–261.

Kootahi, K., Leung, A.K., Wang, Y., 2023a. Modified value stabilization methodology (MVSM) to efficiently determine the sample size required for particle morphology quantification. Powder Technol. 420, 118396.

Kootahi, K., Leung, A.K., Wang, Y., 2023b. An algorithm based on distribution similarity to determine the representative sample size for particle morphology characterization. Comput. Geotech. 162, 105696.

Krumbein, W.C., Sloss, L.L., 1963. Stratigraphy and sedimentation, 2nd edition. W. H. Freeman and Co., San Francisco.

Krzanowski, W.J., 2003. Non-parametric estimation of distance between groups. J. Appl. Stat. 30 (7), 743–750.

Lai, Z., Chen, Q., 2019. Reconstructing granular particles from X-ray computed tomography using the TWS machine learning tool and the level set method. Acta Geotech. 14 (1), 1–18.

Li, L., Iskander, M., 2021. Comparison of 2D and 3D dynamic image analysis for characterization of natural sands. Eng. Geol. 290, 106052.

Li, Y., Otsubo, M., Kuwano, R., 2024a. Elastic waves during continuous triaxial shearing influenced by particle morphology. Soils Found. 64 (2), 101443.

Li, Y., Otsubo, M., Liu, J., Kuwano, R., 2024b. Effect of particle morphology on stress and strain characteristics of granular materials during triaxial compression. Acta Geotech. https://doi.org/10.1007/s11440-023-02190-y.

Li, L., Sun, Q., Iskander, M., 2023. Efficacy of 3D dynamic image analysis for characterising the morphology of natural sands. Géotechnique 73 (7), 586–599.

Liang, H., Shen, Y., Xu, J., Chen, S., 2022. Multiscale morphological effects on stress-dilation behaviors of natural sands: A 3D printing simulation method. J. Eng. Mech. 148 (9), 04022046.

Masad, E., Saadeh, S., Al-Rousan, T., Garboczi, E., Little, D., 2005. Computations of particle surface characteristics using optical and X-ray CT images. Comput. Mater. Sci 34 (4), 406–424.

Microtrac., 2023. Dynamic Image Analysis (DIA). state-of-the-art particle size and shape characterization. https://www.microtrac.com/products/particle-size-shape-analysis/dynamic-image-analysis/ accessed March 2023.

Nguyen, T.T., Indraratna, B., 2020. The role of particle shape on hydraulic conductivity of granular soils captured through Kozeny-Carman approach. Géotech Lett 10 (3), 398–403.

Nie, J.-Y., Cao, Z.-J., Li, D.-Q., Cui, Y.-F., 2021. 3D DEM insights into the effect of particle overall regularity on macro and micro mechanical behaviours of dense sands. Comput. Geotech. 132, 103965.

Payan, M., Khoshghalb, A., Senetakis, K., Khalili, N., 2016. Effect of particle shape and validity of G_{max} models for sand: A critical review and a new expression. Comput. Geotech. 72, 28–41.

Powers, M.C., 1953. A new roundness scale for sedimentary particles. J. Sediment. Res. 23 (2), 117–119.

Rorato, R., Arroyo, M., Andò, E., Gens, A., 2019. Sphericity measures of sand grains. Eng. Geol. 254, 43–53.

Sandeep, C.S., Hernandez, A., Stangeland, K., Evans, T.M., 2023. Shape characteristics of granular materials through realistic particle avatars. Comput. Geotech. 157, 105352.

Sheather, S.J., 2004. Density estimation. Stat. Sci. 19 (4), 588–597.

Sheather, S.J., Jones, M.C., 1991. A reliable data-based bandwidth selection method for kernel density estimation. J R Stat Soc B 53 (3), 683–690.

Suh, H.S., Kim, K.Y., Lee, J., Yun, T.S., 2017. Quantification of bulk form and angularity of particle with correlation of shear strength and packing density in sands. Eng. Geol. 220, 256–265.

Sun, Q., Zheng, J., Coop, W.R., Altuhafi, F.N., 2019. Minimum image quality for reliable optical characterizations of soil particle shapes. Comput. Geotech. 114, 103110.

Wadell, H., 1932. Volume, shape, and roundness of rock particles. J. Geol. 40 (5), 443–451.

Wadell, H., 1933. Sphericity and roundness of rock particles. J. Geol. 41 (3), 310–331.

Xiao, Y., Fang, Q., Stuedlein, A.W., Matthew Evans, T., 2023. Effect of particle morphology on strength of glass sands. Int. J. Geomech. 23 (8), 04023117.

Yang, H.-W., Lourenço, S.D.N., Baudet, B.A., 2022. 3D fractal analysis of multi-scale morphology of sand particles with μCT and interferometer. Géotechnique 72 (1), 20–33.

Zhang, C., Zhao, S., Zhao, J., Zhou, X., 2021. Three-dimensional Voronoi analysis of realistic grain packing: An XCT assisted set Voronoi tessellation framework. Powder Technol. 379, 251–264.

Zheng, J., Hryciw, R.D., 2015. Traditional soil particle sphericity, roundness and surface roughness by computational geometry. Géotechnique 65 (6), 494–506.

Zheng, J., Hryciw, R.D., 2016. Roundness and sphericity of soil particles in assemblies by computational geometry. J. Comput. Civ. Eng. 30 (6), 04016021.

Zheng, J., Sun, Q., Zheng, H., Wei, D., Li, Z., Gao, L., 2020. Three-dimensional particle shape characterizations from half particle geometries. Powder Technol.. 367, 122–132.

Zhou, B., Wang, J., Wang, H., 2018. Three-dimensional sphericity, roundness and fractal dimension of sand particles. Géotechnique 68 (1), 18–30.